Physics of Fluids ARTICLE scitation.org/journal/phf

Multifunctional roles of hairs and spines in old man of the Andes cactus: Droplet distant coalescence and mechanical strength

Cite as: Phys. Fluids **34**, 012003 (2022); doi: 10.1063/5.0066153
Submitted: 9 August 2021 · Accepted: 8 December 2021 ·
Published Online: 4 January 2022

Lakshminath Kundanati,[1] Nicolò G. Di Novo,[1,2] Gabriele Greco,[1] Stefano Siboni,[3] Claudio Della Volpe,[3] Alvise Bagolini,[2] and Nicola M. Pugno[1,4,a)]

AFFILIATIONS

[1] Laboratory for Bioinspired, Bionic, Nano, Meta, Materials and Mechanics, Department of Civil, Environmental and Mechanical Engineering, University of Trento, Via Mesiano, 77, 38123 Trento, Italy
[2] Center for Materials and Microsystems, FBK, Via Sommarive 18, 38123 Trento, Italy
[3] Department of Civil, Environmental and Mechanical Engineering, University of Trento, Trento, Italy
[4] School of Engineering and Materials Science, Queen Mary University of London, Mile End Road, London E1 4NS, United Kingdom

[a)] Author to whom correspondence should be addressed: nicola.pugno@unitn.it

ABSTRACT

Cactaceae have adapted to harsh environments by resisting intense solar radiation, retaining and collecting water. Some cacti species have hairs on them along with distinctive spines to serve different functions. In this study, we characterized the Old Man of Andes cactus (*Oreocereus trolli)*. We examined the surface morphology and estimated roughness and adhesion force of both spines and hairs. They both consist of longitudinal microgrooves. The condensation experiments carried out on spines showed that there is a particular phenomenon of distant coalescence (*DC*): smaller droplets flow totally or partially into larger ones through the microgrooves with consequent accumulation of water in a few large drops. An earlier study (Bintein *et al.*, 2019) has shown that artificial micro-grooved surfaces that exhibit *DC* are more efficient than flat ones at collecting and sliding dew, and thus cactus spines could act as soil dew conveyors. The agreement between our analytical model and experimental data verifies that the flow is driven by the Laplace pressure difference between the drops. This allowed us to obtain a general criterion for predicting the total or partial emptying of the smaller drops as a function of the dynamic contact angles of a surface. With the Wilhelmy method, we determined that hairs are less hydrophilic than spines. We also estimated the mechanical properties of both the spines and hairs to evaluate their possible role in physical defense. This study aids in better understanding the physical attributes and the condensation interaction with microstructures, and suggests some functional roles.

I. INTRODUCTION

In desertic and semi-arid environments, Cacti have evolved the necessary characteristics for survival such as resistance to intense solar radiation, water retention in hot and dry hours, and the efficient collection of water either from the ground or from the air. The cuticle thickness of cacti is one of the major contributing factors in terms of heat protection and water loss (Park, 2002). Some species of cactus have hairs on them along with the distinctive spines (Schlegel, 2009) that were known to protect from predators and were hypothesized as modified leaves or parts of the leaves (Freeman and Beattie, 2008). In general, structural traits such as spines are hypothesized to aid in defense against herbivores (Hanley *et al.*, 2007) and are proved to moderate the amplitude of the diurnal temperature changes of the stem surface (Lewis and Nobel, 1977).

With rare rainfall concentrated in a season, the other main water source is the dew which forms on surfaces during the night via radiative cooling (Zhang *et al.*, 2015; Jia *et al.*, 2019). Natural selection has led to superficial structures of plants (e.g., in leaves and spines) and animals (e.g., insects) that favor the nucleation of dew, its transport, and collection (Malik *et al.*, 2014; Gurera and Bhushan, 2020; Zhang *et al.*, 2021). The cactus species *Opuntia microdasys* (Ju *et al.*, 2012), *Gymnocalycium baldianum* (Liu *et al.*, 2015), and *Opuntia stricta* (Masrahi, 2020) that survive in the desert have hierarchical spines that help in harvesting fog efficiently. These spines were observed to have aligned grooves and barbs that aid in the directional movement of the drops toward the base of the spine. The coalescence of condensate droplets on the conical spine builds up a Laplace pressure difference in the new drop which moves toward the base of the spine, where the stomata collect the water. It was observed that the gradient in the surface roughness results in the variation of the surface energy, leading to the force that drives the drop movement (Yang *et al.*, 2008). Spines with conical shapes are known to give rise to a Laplace gradient and, because of their roughness, they help in directing the water into the stems (Malik *et al.*, 2016). The hairs of the desert mosses *Syntrichia caninervis* exploit these principles to collect water efficiently (Pan *et al.*, 2016). Conical artificial microstructures were proven to aid in the movement of the condensed droplets at the tip to the base because of the Laplace pressure gradient with the aid of the fusion-motion process (Cao *et al.*, 2014). Also, hybrid surfaces with superhydrophilic conical patterns on a superhydrophobic background enhance dew harvesting by combining transport properties and water removal efficiency, respectively (Hou *et al.*, 2020). The surface of a Sarracenia trichome instead exploits the formation of a thin film of water in microchannels followed by the ultra-fast sliding of the drops on it toward the base of the trichome (Chen *et al.*, 2018). Another plant that transports dew quickly *is Nepenthes alata* which uses multi-curvature structures (Li *et al.*, 2020).

The old man cactus of the Andes (*Oreocereus trolli: Cactacea*) has spines and hairs on the surface which are more densely distributed than most of the species of the cacti family. The presence of hairs, called pubescence, is known to reduce the heat load on the leaves and thereby resulting in lower leaf temperatures during the day and lower transpiration (Ehleringer and Mooney, 1978). Experiments performed on the Peruvian Andes by Keeley and Keeley (1989), where the air temperature can be 40 °C during the mid-day and drops to almost −5 °C at night, showed that the hairy form of *Tephrocactus ftoccosus* maintains the subepidermal temperature above 0 °C 3 h longer than the hairless form. As it is important for cacti to defend themselves from herbivores, we evaluated the mechanical characteristics of the hairs and spines. Surface morphological characterization of both hairs and spines was carried out to investigate the role of roughness and other morphological features in the condensation and wetting process. We used different approaches with hairs and spines because of the size and shape of them and the limitation of the experimental set-up. Thus, contact angle measurements of the hairs were performed using the *Wilhelmy method* to investigate their wettability. The primary aspect of this study is to examine the mechanism of condensate growth on the spines. The presence of the micro-grooves longitudinally covering the cactus spines causes a particular type of dropwise condensation, wherein these grooves aid in the formation of water capillaries. If a capillary connects two droplets of different sizes, a relatively slow flow from the small to the big droplet starts. We call it *distant coalescence (DC)* to distinguish it from the common coalescence via contact. *Distant coalescence* was not reported in earlier studies on cacti (Yang *et al.*, 2008; Ju *et al.*, 2012; Malik *et al.*, 2016). It is only reported in a recent study on artificial micro-grooved surfaces with superior ability in collecting dew compared to flat surfaces (Bintein *et al.*, 2019). They showed that soaked grooves connect the small drops to the large ones, that the first flows into the second, and characterized how this phenomenon affects the whole condensation process and accelerates the sliding of the condensate. We performed experiments to quantify the flow of single *distant coalescence* events on the *Oreocereus trolli* spines in terms of instantaneous volume of the droplets involved and duration. We used analytical modeling to validate the hypothesis of a flow through an open microchannel driven by Laplace pressure difference (Bintein *et al.*, 2019). We then investigated the total or partial emptying of small droplets in relation to dynamic contact angles. Thus, investigating the structure-function relations will help in understanding the function of the hairs and spines on cacti and in the design of artificial surfaces that harvest water vapor efficiently.

II. MATERIALS AND METHODS

A. Materials

Old man of the Andes (*Oreocereus trolli)* is a slow-growing species that grows high up in the Andes mountain range (north Argentina and south Bolivia) where the climate is arid and the temperature range during the daytime can be more than 40 °C. Our cactus sample was brought from the local nursery and kept in ambient conditions (21–23 °C during summer and 30%–40% RH, 18–19 °C during winter, and 21%–35% RH). The hairs and spines are extracted from the plant carefully by trimming them.

B. Microscopy

The images of cactus hair were taken using an optical microscope (bx61, OLYMPUS) and a mobile camera (OnePlus 7t, India). The OnePlus 7 T mobile comes with a 48-megapixel Sony IMX586 sensor that has an f/1.6 aperture and has a resolution of 1.6-micron pixels (4-in-1). Images from the microscope were captured using the CCD camera (SC50) which has a pixel size of $2.2 \times 2.2\,\mu$m. The standard calibration slide provided by the microscope manufacturer was used for calibration. The dimensions from the images were reported using the standard scale bar in the microscope which was checked with a calibration.

Scanning Electron Microscopy (SEM) imaging was performed on the separated hair samples. Hair samples were carefully mounted on double-sided carbon tape, stuck on an aluminum stub followed by sputter coating (machine Quorum Q150T) with Pt/Pd 80:20 for 5 min. A FE-SEM (40 Supra, ZEISS, Germany) was used with accelerating voltages between 5 and 20 kV. ImageJ software was used for all dimensional quantification reported in this study (Abràmoff and Magalhães, 2004).

C. Contact angle measurements

The trimmed cactus hairs were carefully glued in the folded aluminum foil to mount it on the clip holder (Fig. 1). Advancing and receding contact angle measurements were performed using a procedure with the use of Wilhelmy method (Della Volpe *et al.*, 2001). For the experiments with water, ultrapure water produced by a Millipore Milli-Q device (18.5 MΩ cm) was used, and it was replaced after each experiment. As shown in Fig. 1, the cactus fiber was pushed and pulled out using a displacement actuator at a rate of 5 μm/s, and the corresponding changes in the force were recorded using a microbalance, which can acquire data at a frequency of 1 Hz. A re-test was performed to observe the re-wetting behavior of the hairs after the first test. We have also carried out additional experiments using a liquid as hexadecane to validate the average value of the fiber diameter. We assumed that the surface of the fiber is smooth and also the diameter is constant

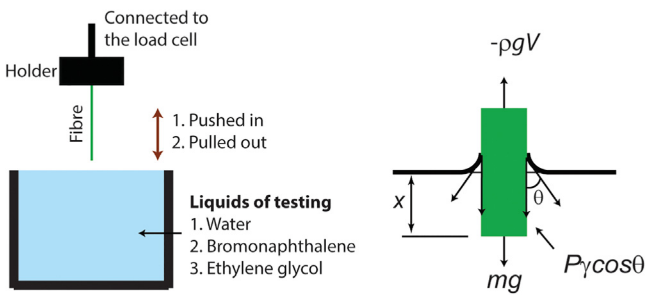

FIG. 1. Schematic of the set-up used for measuring the equilibrium contact angle using Wilhelmy method.

throughout the length to estimate the contact angle through this method.

When the conditions are fully satisfied, we can estimate the contact angle using the following equation:

$$F(h) = mg + P\gamma\cos\theta - \rho g V, \tag{1}$$

where $F(h)$ is the total force measured on the sample, at a depth h, m is the sample mass, P is the fiber perimeter, V denotes the volume of the sample immersed in the liquid of density ρ and surface tension γ, θ is the contact angle at the interface of sample and liquid), and g stands for gravity acceleration. Because the gravitation force (mg) is constant, the equation can be rewritten as

$$F(h) - mg = F_1(h). \tag{2}$$

By extrapolating this equation to zero depth condition, where $V = 0$, we get the following equation from which the constant angle is estimated:

$$F_1(0) = P\gamma\cos\theta. \tag{3}$$

We have used 6 hair samples to perform the contact angle measurements and the re-tests. Bromonaphthalene and ethylene glycol were also used to try to check the acid-base properties of the surface. As later commented, these runs gave contradictory results.

Once the contact angle is obtained using the uniform diameter assumption, the value is inserted in the corresponding equation to estimate the diameter at the specific depth. The conical shape of the fibers has been proven by optical (Table I) and Wilhelmy measurements with the following results; the two methods give coherent results and the very slow variation of the diameter allows to apply a mean-value-diameter in the Wilhelmy estimation of wettability. This introduces a systematic error in the determination of the wettability properties.

TABLE I. Cactus hair dimension measured from an optical microscope.

Cactus hair number	Near base diameter (μm) ~10 mm from the tip	Near tip diameter (μm)
1	38 ± 7	29 ± 6
2	61 ± 6	33 ± 4
3	37 ± 4	29 ± 3
4	57 ± 9	23 ± 5

D. Condensation experiments

We performed the condensation experiments in a custom-made setup (see supplementary material S3 for the setup schematic). We introduce the desired humid air in a chamber (800 cm^3) by mixing a dry air flux and a wet air one (Fig. S1). The wet air flux is humidified with a bubbler of de-ionized water (18 MegaOhm). Each flux is set with a flow meter (FR2000, Key instruments), and the total flux is 800 sccm. The relative humidity (RH) and temperature of the mixed air (T_a) are measured with an Arduino BME280 sensor (accuracies ±3% and ±1 °C) placed at the chamber inlet. $T_a = 24 \pm 1\,^\circ\text{C}$, $RH = 47 \pm 3\%$, and the temperature of the aluminum plate where we place the spines, cooled by a thermostatic bath and two Peltier stages, is $T_p = 2 \pm 0.3\,^\circ\text{C}$ (measured with a thin film PT100 thermocouple, RS pro, class B accuracy) for the duration of the experiments. Thus, the saturation ratio on the plate surface $s = P^{vap}_{amb}/P^{vap}_{sat}(T_p) = 2$, where P^{vap}_{amb} is the water vapor pressure of the mixed air and $P^{vap}_{sat}(T_p)$ is the saturation vapor pressure at T_p. We place the spine on the plate, and we cool it while introducing dry air. When T_p is reached, we introduce humid air and condensation starts. The chamber is equipped with an upper and a lateral quartz window. We recorded videos of condensation with a digital microscope Dino-Lite model AM7915MZTL (working distance of 3 cm at the maximum magnification of ×140).

The rate and density of droplets nucleation and subsequent growth on surfaces depend on the surface temperature, the vapor saturation ratio, and the wettability (Lee *et al.*, 2012; Kalikmanov, 2013; Castillo *et al.*, 2015). Because the natural cooling process of the spines is driven by radiative cooling and complex interactions with time-dependent humidity and temperature airflows, our experiments with the spine cooled by conduction to a certain T_p and exposed to a certain humid air are representative only of a particular natural process leading to the same thermodynamic conditions, excluding time dependencies. On the other hand, a droplets coalescence event (by contact (Narhe *et al.*, 2004; Chu *et al.*, 2017) and at a distance, as we shall see) depends on the wettability and geometry of the droplets regardless of the process that generated them, T_p and s. We placed spines on the plate in two configurations, namely, 1 and 2. (1) In direct contact with the plate. A water film forms between the plate and the spine (Fig. S4), assures a good homogenous thermal contact, and aids in condensation initiation on all the spine simultaneously. The spine temperature is reasonably close to the plate one. The drawback is the risk of unwanted coalescence with condensation on the plate. (2) The spine is placed about 0.3 mm above the plate, embedded in two pieces of soft thermal paste (3 W/mK) distant 2 mm. In this way, there is no interference with plate-droplets, but there is a thermal gradient (not modeled in the spine (Zhu *et al.*, 2020) whereas for the first ~ 15 min the condensation is not homogeneous). However, as our current goal is to describe the dynamics of single distant coalescence events (independent of T_p and s) and not the entire condensation process, we extracted data of droplets asymmetry, flow and emptying condition (as described in the paragraph 3.5) from experiments in both configurations. Side-view experiments in configuration 1 are employed to quantify the DC flows so we can measure the droplets contact radii and heights at each instant. Top-view experiments (in both configurations) serve to evaluate the droplets asymmetry. Side and top-view experiments in both configurations produce data for the emptying condition criterion.

Condensation experiments with hairs are not feasible with our setup due to their small diameter. Indeed, by placing the hair directly on the plate, there is direct coalescence with the droplets on aluminum. By suspending it on thermal paste, we did not observe condensation because the heat conduction in the hair is not sufficient to bring it to the dew temperature. A radiative cooling setup (like the one employed in Trosseille *et al.*, 2021) is needed to investigate condensation on the hairs network and the whole cactus.

E. Mechanical testing

Hair samples were fixed on paper-based holders that aid in holding the sampling between the clamps without causing damage to the specimen. The tests (samples tested = 10) were performed using a nano-tensile testing machine (T150, Agilent, Santa Clara, USA), attached with a transducer of maximum load capacity of 500 mN. Specimens were tested at a strain rate of 0.1%/s.

Spines samples were cut from the plants and tested on the same day. Bending tests were performed on the spines (samples tested = 5) using a custom-built 3-point bending setup made of acrylic. The rate of testing in 3-point bending tests was also kept at 0.01 mm/sec, and a span length of 4.83 mm was used.

F. Atomic force microscopy

Atomic force microscopy (AFM, NT-MDT Smena scanner) was used to obtain the images, topography, and force curves on the samples. The environmental conditions that were controlled included a temperature of 21 °C and relative humidity of 60%, at which the experiments were carried out. Different cantilever tips and operational modalities were used to obtain topography and force curves. Topography was performed using the semi-contact mode by using a NT-MTD NSG-11B tip (10 nm nominal tip radius, resonance frequency of 181 kHz and force constant between 2.5 and 10 N/m), whereas force curves were obtained by using a contact mode tip (NT-MTD, CSG-11B, 10 nm nominal tip radius, 428 kHz resonance frequency and force constant between 0.01 and 0.08 N/m).

The spines and the hairs of the cactus were glued using a double-sided bonding tape on the sapphire AFM sample holder. AFM data were analyzed with the support of Gwyddion and IA_P9 application. Roughness is commonly defined as the height distinctions of the surface at micro/nanoscale scale. R_p and R_v give the maximum height of the peak and a maximum depth of the valley, respectively, and R_z gives the peak-to-peak value. The roughness values were computed both for the average (R_a) value, following British standard ISO 4287:2000. The Wenzel parameters were estimated approximatively as $r_W = A_{scan}/A_{proj}$ where A_{scan} and A_{proj} are the scanned and projected areas, respectively. The current/tip-deflection response curve of the cantilever was calculated starting from the current/distance curves collected on a silicon chip surface and was estimated to be equal to 0.01 A/m for the spine and 0.002 A/m for the hair. The adhesion force (cantilever tip-sample) values were obtained by using the nominal elastic constant of the used cantilevers and by measuring the jump-out current of the tip from the surfaces of the tested sample. Ten curves were obtained for each type of sample.

III. RESULTS AND DISCUSSION

A. Surface morphology and roughness

This species of cactus appears to have hairs and spines of moderate density covered around its stem [Figs. 2(a) and 2(b)]. The top profile view shows that the hairs were able to form outer hair layer about a centimeter away from the stem surface. The hairs and spines originate from the same location, and the hairs from one node appear to get in contact with the hairs from the adjacent nodes [Fig. 2(c)]. The apical spines and hairs in the cactus *Carnegia gigantea* are estimated to bring down the maximum temperature of the meristem by as much as 10 K (Jones and Rotenberg, 2001). The silver shiny cactus hairs also resemble similar types of hairs on ants which were proved to be effective in light reflection and heat dissipation (Shi *et al.*, 2015). This is crucial for desert plants, in which photosynthesis activity can be reduced because they are exposed to intense solar radiation (Koch *et al.*, 2009).

Surface morphology of the hairs was examined using SEM. The surface topography micrographs show that each hair is a bundle of fibers with a smaller diameter embedded together in some matrix, and the surface appears to have wrinkles when observed at higher magnification [Figs. 3(a) and 3(b)]. We have measured the diameter of the hairs at two different locations, near the tip and base regions at distance ~10–12 mm and the respective values were 34.3 ± 5.4 and $42.4 \pm 7\ \mu$m with a mean value of $38.4 \pm 5.5\ \mu$m. Also, the fibers in the hair appear slightly twisted.

The density of spines on the cactus was observed to be much lesser and their average diameter was much larger, as compared to that of the hairs. The surface morphology of the spines appeared similar to that of the hairs, with ridge-like formations running along the length of the spine (Fig. 4).

Surface topography images of both the spines and the hairs show ridges on the surface and the corresponding roughness was estimated from them (Fig. 5). When compared, the local surface roughness estimated from the scans of ~100 μm^2 area of the spines (42 ± 7 nm) was observed to be higher than that of the hairs (29 ± 7 nm) as shown in Table II. The surface roughness scans show that the hairs have slightly lesser deep grooves as compared to the spines, which was also observed in the SEM images. Notably, there are no micro fins on the examined spines, like those present on the spines of other cacti species and observed to be hydrophobic (Malik *et al.*, 2016). Further, these other species of cacti do not have dense hairy structures on the surface along with the spines. The leaves of *Stipagrostis sabulicola* were observed to have long ridges and grooves, which were shown to promote droplets condensation and movement (Roth-Nebelsick *et al.*, 2012). Also, the grooves were known to aid in the rapid shedding of water condensate through a self-sustained cascading coalescence (Sharma *et al.*, 2019).

B. Condensation process and distance coalescence

During experiments on the spines, after a certain time, most of the condensed water accumulated into a few large droplets, and the newly nucleated droplets are continuously sucked into them resulting in bigger droplets. We identified three characteristic regimes of condensation. The first regime is characterized by the usual dropwise condensation with contact coalescence along with the growth of the condensate droplets, and as they advance, some micro-grooves are

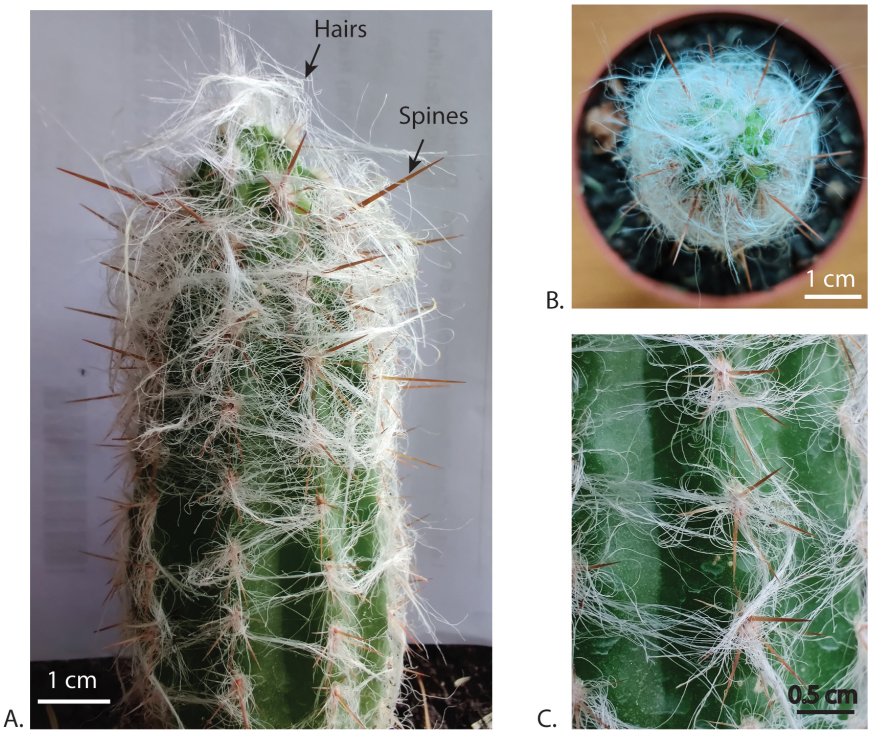

FIG. 2. Optical images of plant. (a) Profile view showing the distribution of hairs and spines, (b) top view, and (c) zoomed in image showing the entangled hairs from one ridge to the other.

filled with water. This can be due to both the imbibition of the grooves from the condensate droplets, as shown by Bintein *et al.* (2019), and the spreading and/or coalescence of tiny droplets growing in the grooves. The second regime starts when the water capillaries establish transportation vessels between droplets and *DC* begins. Smaller droplets flow into the larger ones through the open channels because they have a higher Laplace pressure. The number of droplets then decreases, and at the end, there are a few large drops that are separated clearly. The free surface between these large droplets is eventually repopulated with new condensate nuclei. This is the beginning of regime 3. All the newly grown droplets flow into the large droplets. In this way, all the condensate accumulates in a few drops, in agreement with the literature (Bintein *et al.*, 2019).

In Fig. 6(a), we show two simultaneous distant coalescence events captured by a top-view experiment. They do not appear as contact coalescence events because there is space between the droplets and the characteristic time of emptying is on the order of minutes. In Fig. 7 (Multimedia view), we show the video (accelerated 64 times and at two different magnifications) of a top-view experiment with many distant coalescences to observe both the details of distant coalescence events and the macro distribution of large droplets in regime 3. The limitations of magnification and resolution capabilities of the microscope do not allow to fully characterize the flow of droplets with diameters $<10\,\mu$m. However, we observe that some of those droplets form and disappear before reaching a larger diameter by flowing in the grooves. 8 *DC* flow events were captured in 3 side-view experiments, and the flow analysis

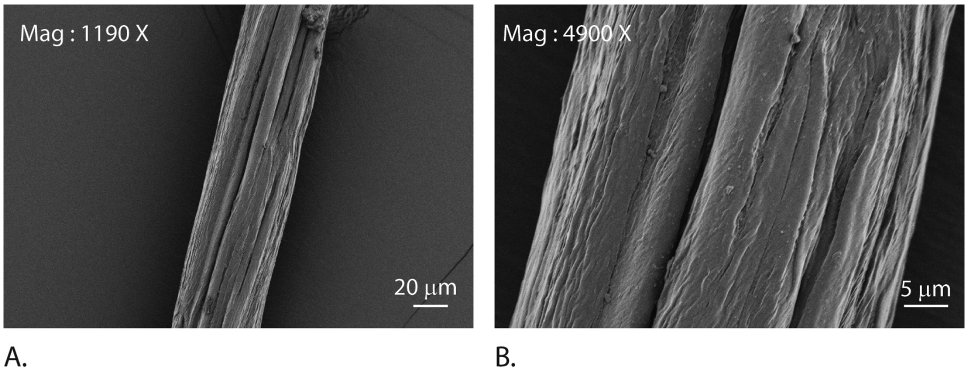

FIG. 3. Scanning electron micrographs of hierarchical hairs at different magnifications.

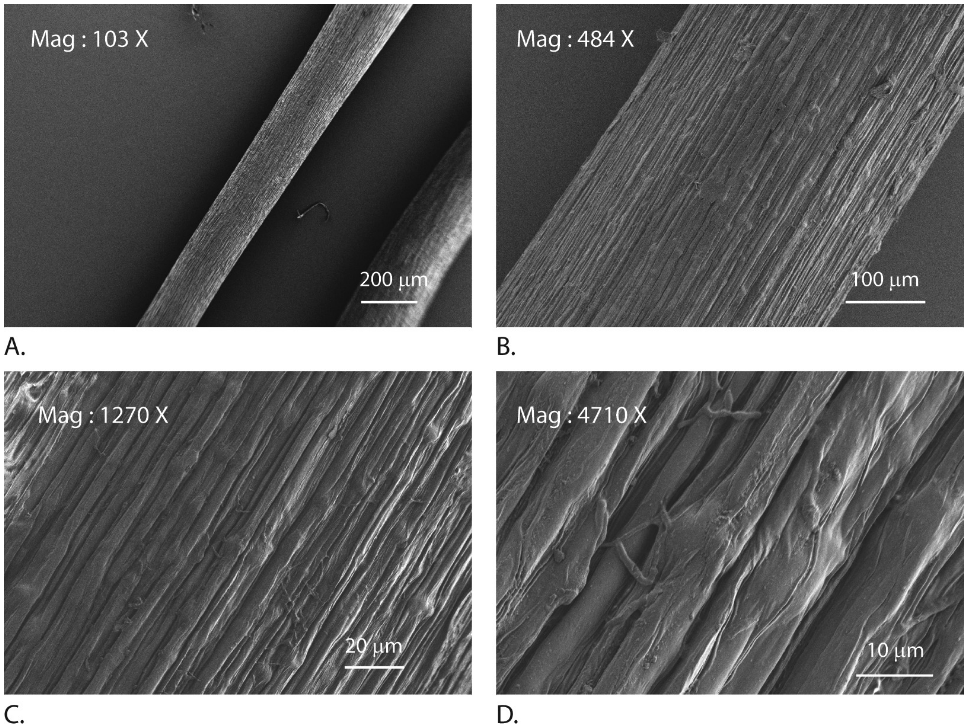

FIG. 4. Scanning electron micrographs of hierarchical spines at different magnifications.

was performed (paragraph 3.5.3) considering the two droplets that are placed symmetrically on the upper edge of the spine [Fig. 6(b)]. As an example, in Fig. 6(b), we show the first event reported in the first side-view experiment (called Exp 1.1 where the first number indicates the experiment and the second the coalescence event shown). In Figs. 8–15 (Multimedia view), we report the videos of Exp. 1.1, Exp. 1.2, Exp. 1.3, Exp. 2.1, Exp. 2.2, Exp. 3.1, Exp. 3.2, and Exp. 3.3, respectively.

C. Analytical model of the flow

To describe the water flow, we modeled the droplets as spherical caps or ellipsoid caps connected by an open microchannel. We simplified the problem by making the following assumptions:

- The surface is smooth without microstructures apart from the channel involved in the flow.
- The water flows through a single channel even if in principle more than one channel could be involved.
- The liquid inside the channel is assumed to be incompressible, the flow Newtonian and laminar.
- The spine curvature is neglected. Considering a planar surface, we can use the spherical or ellipsoidal cap as a model of the droplet. The more the radius of the drops approaches that of the spine, the coarser the approximation.
- The droplets maintain a constant contact radius (thus the contact angle is accordingly changing). As experimentally observed, contact radii change when droplets recede or advance. Thus, the present model describes the flow in each time interval where the contact radii are constant.

We model the flow of a droplet with a pressure-driven term described by the Poiseuille law and a term accounting for the volume rate of condensation,

$$\frac{\Delta P(t)}{R_{flow}} + Q_{cond} = \frac{dV}{dt}, \tag{4}$$

where Q_{cond} is the volumetric flow of condensation, dV/dt is the total volumetric flow, and R_{flow} is the flow resistance inside the channel which depends on its geometry and the fluid considered, namely (Melin *et al.*, 2005),

$$R_{flow} = \frac{3\mu L}{WH^3}, \tag{5}$$

where μ is the fluid (here water) dynamic viscosity, and L, W, and H are the channel length and width, respectively, of an open channel with rectangular cross section and H is the liquid level of the meniscus with a flat interface. Figure 16 shows the scheme of the system. The flow is driven by the pressure difference between the two droplets,

$$\Delta P(t) = P_{small}(t) - P_{large}(t) = \Delta P_{Laplace,\,small}(t) - \Delta P_{Laplace,\,large}(t), \tag{6}$$

wherein general the Laplace pressure is

$$\Delta P_{Laplace} = \gamma\left(\frac{1}{R_1} + \frac{1}{R_2}\right), \tag{7}$$

with R_1 and R_2 being the main curvature radii and γ is the liquid surface tension. Equation (4) is solved by expressing the parameters of

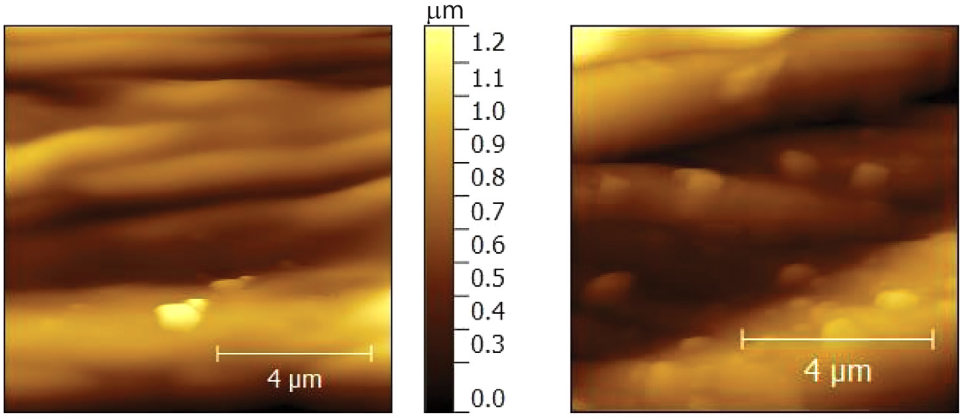

A. Spine

B. Hair

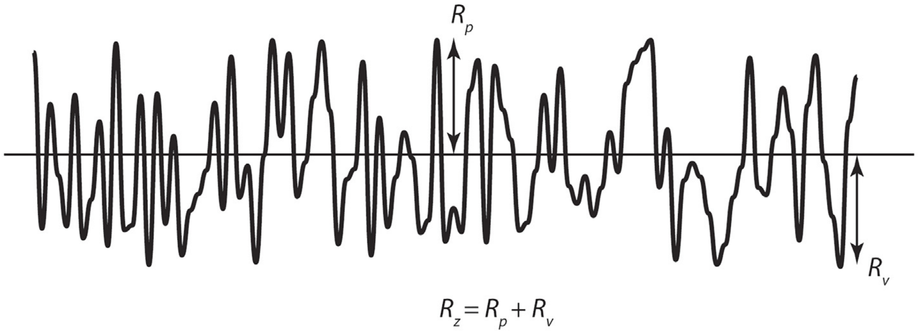

C. Roughness parameters representation

FIG. 5. Surface topography images from the AFM measurements. (a) Spine, (b) hair, and (c) schematic representation of roughness parameters.

the equation as functions of variables that are experimentally measurable. The experimental data extracted from the videos are the droplets contact radii, heights, and the distance between the contact lines (L).

1. Modeling with spherical caps

Modeling the system as a flow between two spherical caps through the microchannel is a good compromise between simplicity and relevance to the phenomenon. Being spheres, $R_1 = R_2 \equiv R$. We call r_s and h_s the contact radius and height of the small droplet, while r_l and h_l are those of the large one. Using the spherical cap approximation, we can express the curvature radius R and the volume of a spherical sessile droplet as

$$R = \frac{h^2 + r^2}{2h}, \tag{8}$$

$$V = \frac{\pi}{6} h (3r^2 + h^2). \tag{9}$$

The flow rate of a growing spherical cap (large droplet) with a constant contact radius is

$$\frac{dV}{dt} = \frac{\pi}{2}(r^2 + h^2)\frac{dh}{dt}. \tag{10}$$

For a spherical cap that empties (small droplet), the flow rate is $-\frac{dV}{dt}$. We measured a constant volumetric flow rate per unit area q_{cond} in side-view experiments; thus, $Q_{cond} = q_{cond} A_{cont}$ with A_{cont} the droplet contact area. Inserting Eqs. (7), (8), and (10) inside (4) for both droplets, we obtain two coupled differential equations,

TABLE II. Measured roughness values of the surfaces of the hairs or spines.

Sample	Roughness average, R_a (nm)	Maximum height of the roughness R_z (nm)	Maximum roughness valley depth R_v (nm)	Maximum roughness peak height R_p (nm)	Wenzel parameter (pure number)
Hairs	29 ± 7	128 ± 46	117 ± 43	104 ± 58	1.172 ± 0.081
Spines	42 ± 7	144 ± 23	146 ± 25	106 ± 42	1.068 ± 0.029

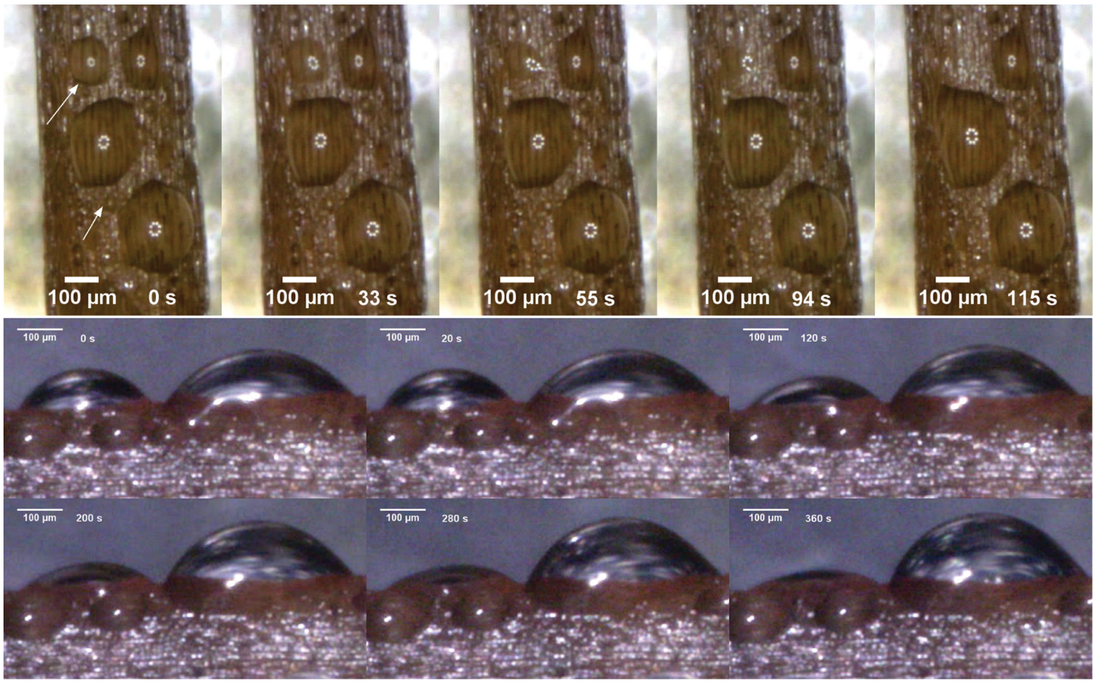

FIG. 6. (a) Top-view experiment. The white arrows indicate the two droplets that empty. (b). Frames of the side-view Exp 1.1.

$$-2\frac{\gamma}{R_{flow}}\left(\frac{2h_s}{h_s^2+r_s^2}-\frac{2h_l}{h_l^2+r_l^2}\right)+q_{cond}\pi {r_s}^2=\frac{\pi}{2}\left(h_s^2+r_s^2\right)\frac{dh_s}{dt}, \qquad (11)$$

$$2\frac{\gamma}{R_{flow}}\left(\frac{2h_s}{h_s^2+r_s^2}-\frac{2h_l}{h_l^2+r_l^2}\right)+q_{cond}\pi {r_l}^2=\frac{\pi}{2}\left(h_l^2+r_l^2\right)\frac{dh_l}{dt}. \qquad (12)$$

Solving numerically these equations in MATLAB, using as initial conditions the initial experimental heights, we obtain the time evolution of heights that can be compared with experimental data. If $r_l \gg r_s$, which means $\Delta P_{Laplace,\,small}(t_0) \gg \Delta P_{Laplace,\,large}(t_0)$, the solution tends to the analytical one proposed by Berthier and Beebe (2007) with $\Delta P(t) = \Delta P_{Laplace,\,small}(t)$. However, this would be an approximation not acceptable for the system under analysis because $\Delta P_{Laplace,\,small}(t_0) \approx (2 \div 10)\cdot\Delta P_{Laplace,\,large}(t_0)$, and the flow depends on the instantaneous configuration of both the droplets. Experiments show that the two droplets reach an equilibrium configuration after the flow. In the discussion section, we see that the model solutions provide the equilibrium condition when the Laplace pressures become equal (the heights reach two distinct values). However, this is not observed in all the cases, specifically, when the small droplet has a contact radius sufficiently smaller than the large droplet one and empties.

FIG. 7. Video of the top-view condensation experiment accelerated 64 times. In the first 16 seconds (higher magnification), there is the transition between regime I and II with the first distance coalescence events. Then, a few large droplets remain, and all the re-nucleated ones are continuously sucked into them (regime III). (Multimedia view: https://doi.org/10.1063/5.0066153.1)

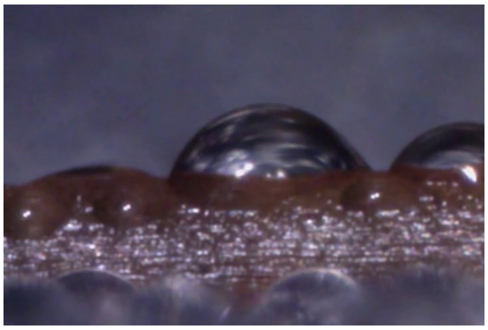

FIG. 8. Video of the side-view experiment Exp. 1.1, accelerated 32 times. (Multimedia view: https://doi.org/10.1063/5.0066153.2)

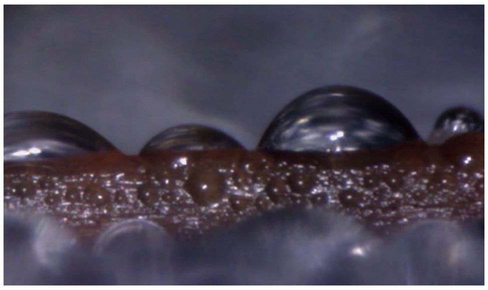

FIG. 9. Video of the side-view experiment Exp. 1.2, accelerated 32 times. (Multimedia view: https://doi.org/10.1063/5.0066153.3)

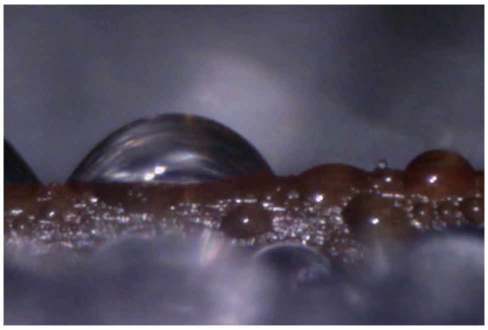

FIG. 10. Video of the side-view experiment Exp. 1.3, accelerated 2 times. (Multimedia view: https://doi.org/10.1063/5.0066153.4)

2. Modeling with ellipsoid caps

Top view experiments give us information on the droplet shape and clearly show that larger droplets are like ellipsoid caps. There are two main contact radii: the one longitudinal to the axis of the spine, r_{long}, which can be measured from the side view experiments, and the transversal one, r_{tran}, which can be measured only from the top view. Because the flow experiments are from the side view, the two radii are related to estimate r_{tran} using the measured r_{long}. Thus, the two radii of some droplets are measured in two top-view experiments. The droplets are nearly spherical when small but change into ellipsoidal with an increase in volume. Normalizing the radii with the spine radius $D/2$ (where D is the mean spine diameter) and fitting them to a parabola [Fig. 17(a)], we obtained a useful phenomenological equation,

FIG. 11. Video of the side-view experiment Exp. 2.1, in real time. (Multimedia view: https://doi.org/10.1063/5.0066153.5)

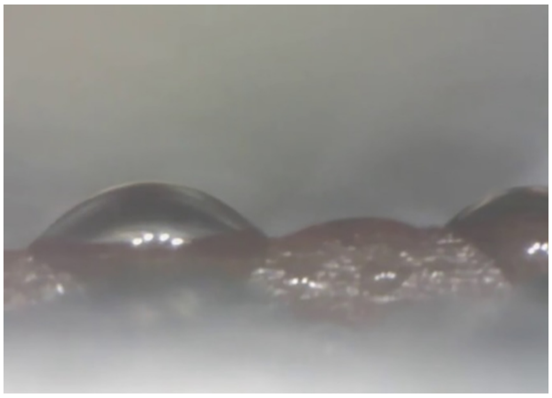

FIG. 12. Video of the side-view experiment Exp. 2.2, accelerated 64 times. (Multimedia view: https://doi.org/10.1063/5.0066153.6)

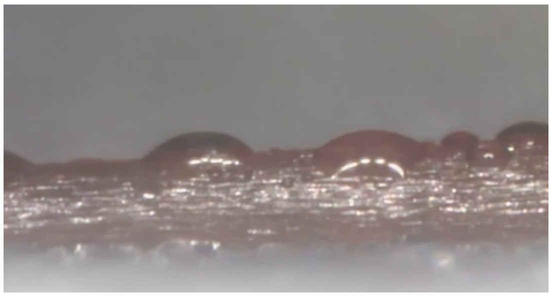

FIG. 13. Video of the side-view experiment Exp. 3.1, in real time. (Multimedia view: https://doi.org/10.1063/5.0066153.7)

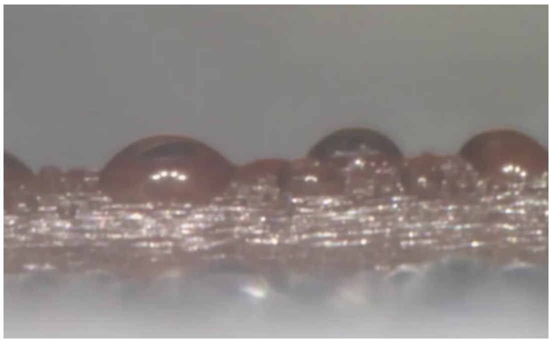

FIG. 14. Video of the side-view experiment Exp. 3.2, accelerated 16 times. (Multimedia view: https://doi.org/10.1063/5.0066153.8)

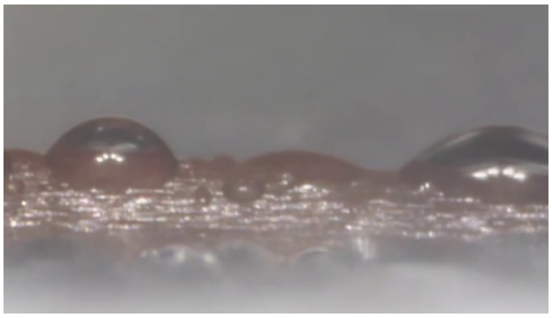

FIG. 15. Video of the side-view experiment Exp. 3.3, accelerated 32 times. (Multimedia view: https://doi.org/10.1063/5.0066153.9)

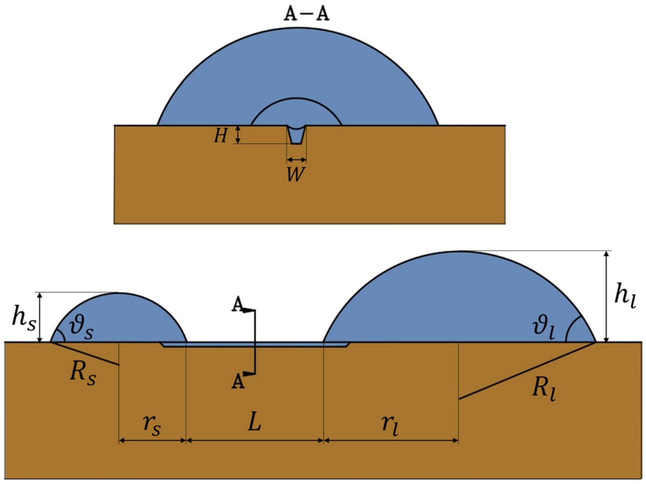

FIG. 16. Scheme of the system from the transversal (top) and longitudinal (bottom) view with respect to the axis of the spine.

$$\frac{2\,r_{tran}}{D} = -0.2575\left(\frac{2\,r_{long}}{D}\right)^2 + 0.9919\left(\frac{2\,r_{long}}{D}\right). \tag{13}$$

We write Eq. (4) for the two droplets considering them as ellipsoidal caps by expressing the volumetric flow and the curvature as a function of measurable variables. The volume of an ellipsoidal cap is

$$V = \frac{\pi f b h^2}{3c^2}(3c - h), \tag{14}$$

where c is the semi-axis perpendicular to the surface of the spine, b is the one parallel to the spine axis, f is one of the transversal directions, and h is the height of the cap defined as c-X [Fig. 17(b)].

To determine the semi-axes, we use an experimental observation. The shape of the droplets recorded in side-view experiments is analyzed considering the plane zOy [Fig. 17(b)] with the "Contact angle" plug-in of ImageJ. These droplet profiles are well-fitted with a circular shape and thus satisfy the assumption $c = b$. For the term $\Delta P(t)$ of Eq. (4), we need the Laplace pressures of the two droplets thus using the general Eq. (7) with the two radii of curvature, $R_1 = R_{long}$ and $R_2 = R_{tran}$. Thus, R_{long} is simplified as follows:

$$c = b = R_{long} = \frac{r_{long}^2 + h^2}{2h}. \tag{15}$$

To determine f, we consider the ellipse identified by the intersection between the ellipsoid and the surface (plane surface, as assumed at the beginning). The equation of that ellipse is

$$\frac{x^2 c^2}{f^2 h(2c - h)} + \frac{y^2 c^2}{b^2 h(2c - h)} = 1. \tag{16}$$

For $y = 0$, $x = r_{tran}$ and with Eq. (16), we get

$$f = \frac{r_{tran}}{r_{long}}\left(\frac{r_{long}^2 + h^2}{2h}\right). \tag{17}$$

Finally, by inserting Eqs. (15) and (17) in (14) and calculating the derivative with respect to time, we obtain the flow rate of an ellipsoidal cap for constant contact radius,

$$\frac{dV}{dt} = \frac{\pi}{2}\cdot\frac{r_{tran}}{r_{long}}\left({r_{long}}^2 + h^2\right)\frac{dh}{dt}. \tag{18}$$

Regarding the second radius of curvature, R_{tran}, we need another approximation. Since the intersection of the ellipsoid with the plane xOz generates an ellipse, a unique radius of curvature is not possible. We consider R_{tran} as the radius of the circle that intersects the plane of the spine forming a circular segment having a chord equal to $2r_{tran}$ and with height equal to h, i.e.,

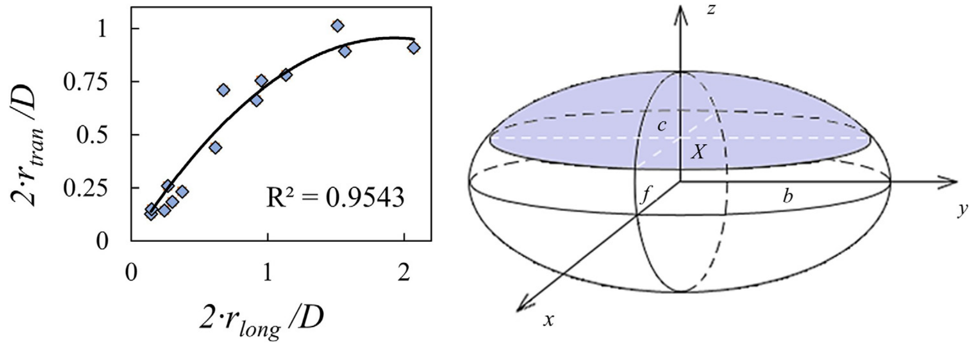

FIG. 17. (a) Normalized longitudinal and transversal contact radii. As captured by the curve, $2\,r_{tran}$ does not exceed D for the cases of interest. Droplets bigger than the spine would be far outside the assumption of planar surface. (b) Scheme of a general ellipsoidal cap.

$$R_{tran} = \frac{r_{tran}^2 + h^2}{2h}, \tag{19}$$

that is, a curvature radius in between the two principal curvature radii of the mentioned ellipse. Again, by writing Eq. (4) with these terms for both the droplets, we obtain a system of two coupled differential equations of the ellipsoidal caps heights,

$$-\frac{\gamma}{R_{flow}}\left(\frac{2h_s}{h_s^2 + r_{s,long}^2} + \frac{2h_s}{h_s^2 + r_{s,tran}^2} - \frac{2h_l}{h_l^2 + r_{l,long}^2} - \frac{2h_l}{h_l^2 + r_{l,tran}^2}\right) + q_{cond}\,\pi\, r_{s,long} r_{s,tran} = \frac{\pi}{2}\cdot\frac{r_{s,tran}}{r_{s,long}}\left({r_{s,long}}^2 + {h_s}^2\right)\frac{dh_s}{dt}, \tag{20}$$

$$\frac{\gamma}{R_{flow}}\left(\frac{2h_s}{h_s^2 + r_{s,long}^2} + \frac{2h_s}{h_s^2 + r_{s,tran}^2} - \frac{2h_l}{h_l^2 + r_{l,long}^2} - \frac{2h_l}{h_l^2 + r_{l,tran}^2}\right) + q_{cond}\,\pi\, r_{l,long} r_{l,tran} = \frac{\pi}{2}\cdot\frac{r_{l,tran}}{r_{l,long}}\left({r_{l,long}}^2 + {h_l}^2\right)\frac{dh_l}{dt}. \tag{21}$$

3. Comparison of model with experimental data

The experimental data of 8 distant-coalescence events captured in 3 side-view experiments are analyzed. For each event, we extracted an appropriate number of frames and measured h_s, h_l, r_s, r_l, and L with ImageJ software. The measured variables and the comparison of measured and simulated heights of the eight events are available in supplementary material S1.1 and S1.2, respectively, and in Fig. 19. To determine the channel profile needed for the calculation of R_{flow}, we observed a spine cross section by optical microscopy: it can be assimilated either to a truncated cone or a rectangle. The range of the widths W between the ribs top is $5 \div 14\,\mu$m. The ratio $\frac{W}{H_g} = 2.0 \pm 0.6$(whit H_g the height of the groove from the ribs top to the channel bottom). The capillary meniscus may assume either a swollen or a concave shape depending on the flow conditions (pressure, flow rate) as reported for rectangular open microchannels (Melin *et al.*, 2005). Moreover, having the grooves a non-constant cross section [Figs. 3(c), 3(d), and 5(a)], a certain contact angle, rounded top of the ribs, and tapered walls, we expect a variable meniscus along the capillary and in time; thus, there is a non-constant R_{flow}. Given these inherent complexities and uncertainties, we simplified by considering the liquid level H to be constant and equal to $W/2$; we used Eq. (5) valid for rectangular open channels with a flat interface and chose the values of W (and therefore H) on the order of the measured ones in order to better fit the flows. Although a slight variation of the chosen W (Table S5) considerably influences the transitory time, it should be noted that it does not affect the final equilibrium configuration of the two droplets (only dependent on the contact radii) which is our present goal. We calculated the condensation volume rate per unit area $q_{cond} = 2.35 \cdot 10^{-8} \pm 0.9 \cdot 10^{-8}$ m/s by analyzing the volume variation of droplets that do not coalesce (via contact or at distance) in side-view experiments. Table S5 lists the values of the parameters L, W, and contact radii for each event. In Figs. 18(a) and 18(b), we report water capillaries length of 50 *DC* events and the length of grooves measured from SEM images of the spine, respectively. We observed a bimodal distribution of capillary lengths: longer channels are typical of

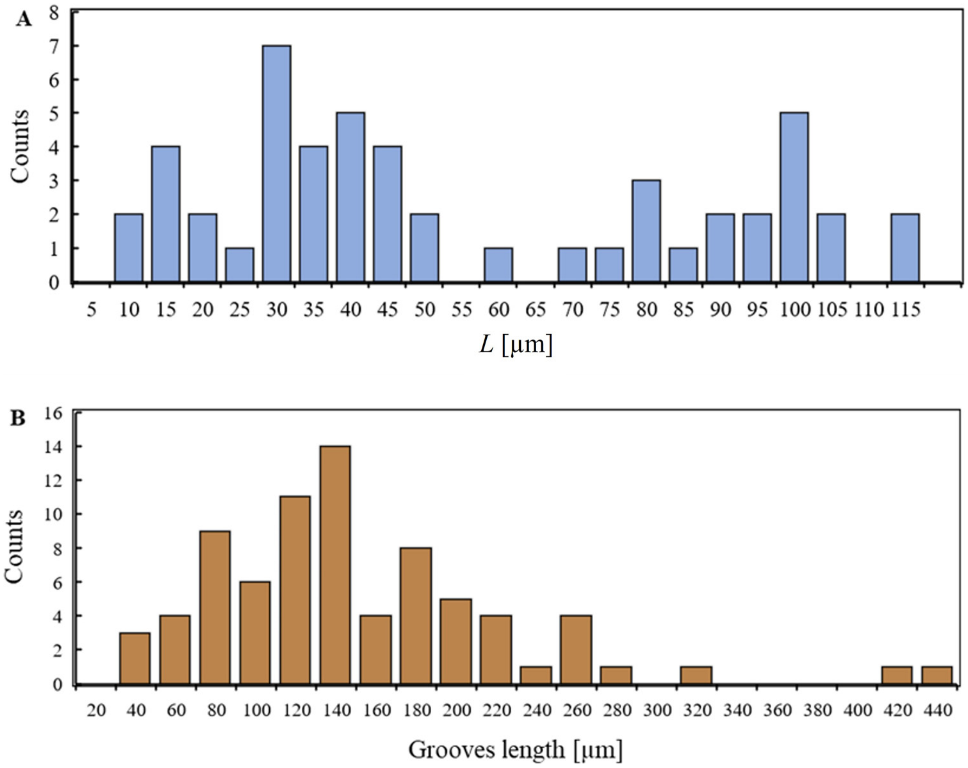

FIG. 18. (a) Water capillaries length measured for 50 DC events recorded in both sides and top-view videos. (b) Groove lengths measured from SEM images of the spine.

regime III where the droplets re-nucleate in the free space between the few large ones and flow into them, while the shorter channels are typical of both regimes II and III where the droplets are closer because of the initial nucleation and dropwise condensation. The length of the water capillaries is clearly limited by the grooves one.

In Fig. 19, we compare the experimental heights with the simulated ones for three representative events. Figure 19 also shows the measured contact radii, calculated curvature radii [Eq. (8)], and contact angles [Eq. (22)] for the case of Exp 3.3 (refer to supplementary material for additional data),

$$\vartheta = \sin^{-1}\left(\frac{r}{R}\right) = \sin^{-1}\left(\frac{2hr}{h^2 + r^2}\right). \qquad (22)$$

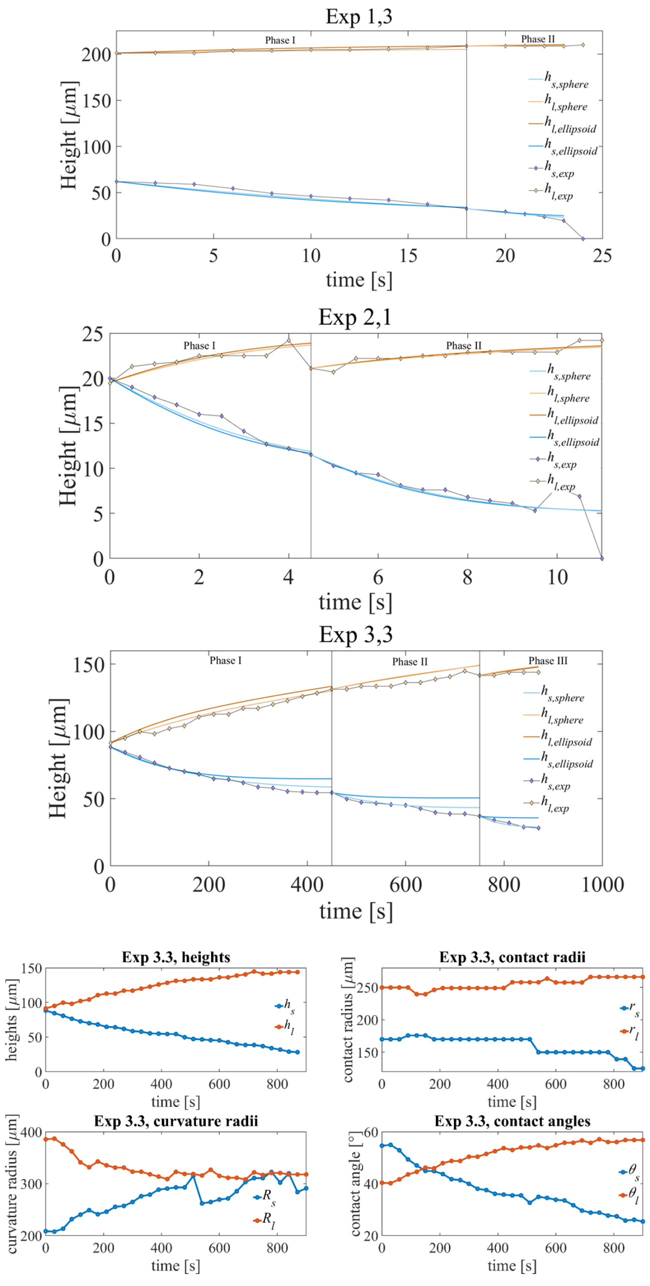

FIG. 19. Comparison of measured and simulated heights evolution of *three distant coalescence* events called Exp 1.3, Exp 2.1, and Exp 3.3. For Exp 3.3, we also show the contact radii, longitudinal curvature radii, and contact angles.

The following observations refer to the spherical cap assumption but are also applicable to the ellipsoidal ones. For Exp 1.3, the hypothesis of constant contact radii stands during phase I and the curvature radii converge toward the same value (see S1.1). Then, at $t = 18$ s, the small droplet recedes, r_s and R_s decrease abruptly, the pressure difference increases, and curvature radii start to converge again. We simulated phase II with the updated contact radii. The system evolves toward a new final configuration, and, at $t = 23$ s, the drop recedes again and empties completely. Similarly, in Exp 2.1, large droplet advances one-time, small droplet recedes two times, and at the end, it is completely sucked into the large one (S1.1). In Exp 3.3, the small droplet recedes and the large one advances two times (S1.1). Three phases can be distinguished, and it is easier to visualize plateaus. We simulated the three phases updating the contact radii after each contact line recession or advancement. At the end of phase I, curvature radii are almost the same, and the flow is almost stopped. Then, the small droplet slides, and a pressure difference is reestablished (curvature radii diverge) and the flow starts again. In this case, however, the system reaches a stable equilibrium in phase III without total emptying of the small droplet.

The comparison between the models and experiments supports the model's validity in each sub-period with constant contact radii, and the plots of the height are a representation of volumes [see Eq. (9)]. Thus, in the DC events which have good agreement between experimental and calculated heights, the volume flow from one droplet to the other is conserved. In two cases, Exp. 1.1 and Exp. 2.2 (see S1.1 and S1.2), the final height of small droplet in Phase II is lower than the simulated one; however, the measured $R_{s,\,long}$ and $R_{l,\,long}$ become equal before the end of phase II. Therefore, the continuation of the flow may be because the large drop coalesces with some other drop on the back of the spine with respect to the direction of observation or out from the microscope field of view, consequently widening $R_{l,\,tran}$ and establishing again a pressure difference. Indeed, top-view experiments show large droplets coalescing (via contact or at distance) simultaneously with more than one droplet and/or with tiny droplets (diameter $<10\ \mu$m).

It is a kind of stick and slip dynamics governed by pinning and depinning similarly to the one reported for evaporating droplets characterized by an oscillating contact angle (Orejon *et al.*, 2011). In general, droplets maintain the contact radii for a certain time and then slip. However, it appears to be more complex in our case because dynamic contact angles vary in the different phases, and thus, we chose to simulate the flow in each sub-phase where the hypothesis of constant contact radii holds. Considering the small droplets in Exp 3.3, ϑ_s decreases to the receding angle $\vartheta_{rec,I}$, the droplet slips a certain length, but ϑ_s continues to decrease until it reaches a new smaller $\vartheta_{rec,II}$, and then slips again and ϑ_s decreases again, vice versa for the large droplets. The variability of the dynamic angles is observed in all the Exp where the contact radii span on an order of magnitude. Hence, we do not believe that it depends on the relative size of the drops and grooves. Rather, experimentally, the dynamic contact angles depend on the droplet inflation and deflation flow rate if $Q > 0.05\ \mu$l/s because inertial effects become relevant (Huhtamäki *et al.*, 2018). For smaller Q, the dynamic angles just depend on surface properties. During distant coalescence, the pressure difference of the drops is a decreasing function and so is Q, as deduced from Eq. (4). Indeed, in the first phases, the inertial effects of the liquid lead to a larger ϑ_{rec} and a smaller ϑ_{adv} compared to the following phases where Q is low and inertial effects become negligible. The ϑ_{rec} and ϑ_{adv} considered as dynamic contact angles without inertial effects are those attained by the droplets in the final phases of the flow. We measured $\vartheta_{rec} = 23.8° \pm 4°$ and $\vartheta_{adv} = 60.7° \pm 5°$. Regarding the two geometries considered we can say that, according to Fig. 17(a), for small contact radii, the approximation with the ellipsoids tends to that with the spheres. For larger drops, in principle, the ellipticity is more pronounced and the model with ellipsoids is preferable (as seen in Exp 1.2 and Exp 2.2-Phase I) even if for the Exp 3.3 the one with the spheres seems more accurate. This discrepancy could be related to experimental errors to coalescence with other droplets not tracked or to the approximation of a flat surface instead of a curved one.

4. Emptying condition

Exp 1.3 and 2.1 are particular because the small droplets are empty at the end. These are events representative of what frequently happens in regime III where all the small drops are sucked into a few large ones. r_l is so much larger than r_s that the small drop should have a contact angle lower than ϑ_{rec} to have the same radius of curvature R_s (and thus Laplace pressure). This does not happen in this cases: when in the final phase (small Q and thus the minimum ϑ_{rec}), the small drop reaches ϑ_{rec} but R_s is still smaller than R_l, the flow continues, and the small droplets recedes and will never be able to reach equilibrium, thus emptying itself completely. Indeed, r_s decreases during a slip, which implies an even smaller R_s when ϑ_{rec} is reached again. One can find a general critical ratio of final contact radii k_{crit} that determines whether the small droplet empties completely or not. Given two contact radii, the most favorable configuration for not having emptying is the one with the large droplet close to the advancement and the small one to a recession which corresponds to the smallest R_l and the largest R_s possible. To avoid emptying, it is needed that $R_s^{rec} \geq R_l^{adv}$ and vice versa. With Eq. (22) it becomes

$$k_{crit} \equiv \frac{r_s}{r_l}\left\{\begin{array}{ll} \geq \dfrac{\sin\vartheta_{rec}}{\sin\vartheta_{adv}} \cong 0.46, & \textit{partial emptying} \\ < \dfrac{\sin\vartheta_{rec}}{\sin\vartheta_{adv}} \cong 0.46, & \textit{total emptying} \end{array}\right\}. \tag{23}$$

Tiny droplets in regime III shown in the top-view experiments and side-view Exp 1.3, 2.1, and 3.1 have $k_{crit} < 0.46$ and indeed flow inside the few large ones and empty completely. Instead, $k_{crit} \geq 0.46$ holds for the other events and, indeed, the systems reach equilibrium without total emptying. In Fig. 20, we compared the prediction of total or partial emptying [Eq. (23)] with distance coalescence events recorded in side-view and top-view experiments. 92% of the events are well predicted (blue dots). In general, considering as the contact angle hysteresis $\Delta\vartheta = \vartheta_{adv} - \vartheta_{rec}$, $k_{crit} = \sin(\vartheta_{adv} - \Delta\vartheta)/\sin(\vartheta_{adv})$ is a decreasing function of $\Delta\vartheta$ for every ϑ_{adv}. The smaller the $\Delta\vartheta$, the closer k_{crit} is to 1, thus maximizing the total emptying events and speeding up the volume accretion of large droplets. Furthermore, as is well known, the lower the $\Delta\vartheta$, the lower the critical volume for the sliding of a drop.

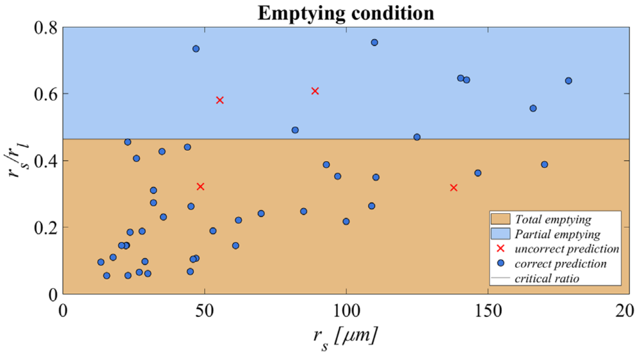

FIG. 20. The critical ratio identifies the two areas of total and partial emptying. Blue dots indicate the distant coalescence events correctly predicted by Eq. (23) and red crosses indicate the non-predicted events. The number of DC events analyzed is 50.

We can say that minimizing $\Delta\vartheta$ would be a good strategy for the optimization of artificial surfaces for the collection of condensate. On the other hand, it is not obvious what an optimal ϑ_{adv} value can be since the contact angle of the surface would also affect the imbibition of the grooves and the stability of the drops. Future experiments on engineered surfaces may shed light on these problems.

5. Hypothesis of advantages

The conical spines of the *Oreocereus trolli* apparently do not serve the function of directing dew toward the stomata as reported for other cactus because we do not observe a net movement of droplets during condensation (Ju *et al.*, 2012; Malik *et al.*, 2014, 2016; Chen *et al.*, 2018). Rather, we can hypothesize that distant coalescence allows large droplets to rapidly reach the critical size to slip or detach toward the ground and thus increase the efficiency of water collection from the roots. To observe the sliding, we did a preliminary experiment by directing a commercial humidifier toward the entire cactus as a whole system made of spine, hairs, and stem. The humidifier has a high-water flux which is not comparable with previous experiments and directs aerosols toward the cactus. In Fig. 21, the cactus is shown after 18 minutes of aerosol and after 30 min, an instant before the bigger droplet slips.

Figure 21(a) shows the third regime with few large droplets on the hairs and spines. After distant and contact coalescences, a single large droplet is formed [Fig. 21(b)]. The droplet slides after reaching a diameter ≈ 2.7 mm. Also, droplets on the densely packed hairs do not slide until they reach similar dimensions. Analogously to the study (Bintein *et al.*, 2019), if the condensation rate in the natural environment during the night is sufficient for the large drops to reach this critical dimension, the phenomenon of *DC* could bring a significant advantage in terms of water droplets reaching the roots compared to flat spines. Future experiments in radiative cooling chambers, where there is dew nucleation and no aerosol deposition could measure the dew collected by a single appendage and better identify the hairs role in this process.

In addition, the accumulation of dew in a few large drops instead of a population of droplets (like in common dropwise condensation with contact coalescence) is peculiar and has a consequence on the subsequent evaporation, after the sunrise. Assuming a constant evaporation mass rate $\dot{m}$, the evaporation time $\tau_E = \rho_{water} V/\dot{m}$ of a sessile droplet is proportional to r^2. In Fig. 22, calculating the evaporation

FIG. 21. (a) Cactus after 18 min and (b) 30 min of aerosol directed toward hairs and spines (The arrow points a large droplet an instant before sliding). The ruler is in the focal plane of the drop, and the black lines are 1 mm apart.

mass rate $\dot{m}$ of a sessile water droplet with the simplified model of Larson *et al.* (Hu and Larson, 2002) valid for hydrophilic surfaces, we show τ_E vs r for sessile droplets with initial contact angle of 60° and exposed to different environmental conditions of temperature and relative humidity (*RH*).

A population of droplets given by the common dropwise condensation would evaporate earlier than a single drop of the same overall volume. Since evaporation of water cools the surface and surrounding air, prolonged evaporation delays the cooling of the hair's microenvironment. In this view, we hypothesize that this accumulation in large droplets may have the following advantages: (1) there is a gradual increase in temperature of the cactus stem due to the radiation exposure after sunrise, and (2) the drops grow during the night, and remain long after sunrise. This water source could attract bats, moths, bees, and birds which consequently help in the pollination of cacti such as *Pilosocereus leucocephalus* and *Pilosocereus* (Munguía-Rosas *et al.*, 2010; Lendel, 2013; Farner and King, 1971; Shawki *et al.*, 2005). Instead, the old man cacti of the Andes, like *Oreocereus celsianus* and *doelzianus,* have diurnal flowers and are pollinated mainly by hummingbirds (Lendel, 2013).

D. Adhesion force and contact angle

The surface adhesion forces of the hairs and spines were measured with the help of AFM experiments. Representative curves from these experiments are shown in Fig. 23, where the adhesion force is measured from the retraction curves. The adhesion force of the hair was measured to be 3.7 ± 0.5 nN, whereas that of the spine was measured to be 0.9 ± 0.1 nN.

Our measurements by the Wilhelmy method show good repeatability in the contact angle values in both the tests performed on the fresh hairs and the re-tested ones (Table III). In the re-tests, where samples were tested the second time after the first test, we have found that the values of both the advancing and receding angles have increased. Thus, the average apparent contact angle of the fresh cactus hairs is 67°. Therefore, the cactus hairs appear to be hydrophilic by nature. Grooved surfaces with a contact angle greater than 45° were found to promote condensation of stable drops on the surface without spreading along the groove due to capillary action (Seemann *et al.*, 2005). In addition, the evaporation of water droplets suspended on the hairs can result in a partial cooling effect around the densely packed hair regions and thereby reduce the heat loss from the surface of the cactus stem directly (Shirtcliffe *et al.*, 2009).

Simple experiments of relatively large droplets placement on the hairs showed that they remain in the position for long time in quite spherical shapes and they do not move toward the stem surface [Fig. 24(a)]. This equilibrium of droplets suspended over single hairs and bundles of hairs is possible, thanks to the 3 D arrangement of hairs and the dynamic contact angles range. [Fig. 24(b)]. From these simple observations and the aerosol deposition and accumulation, we

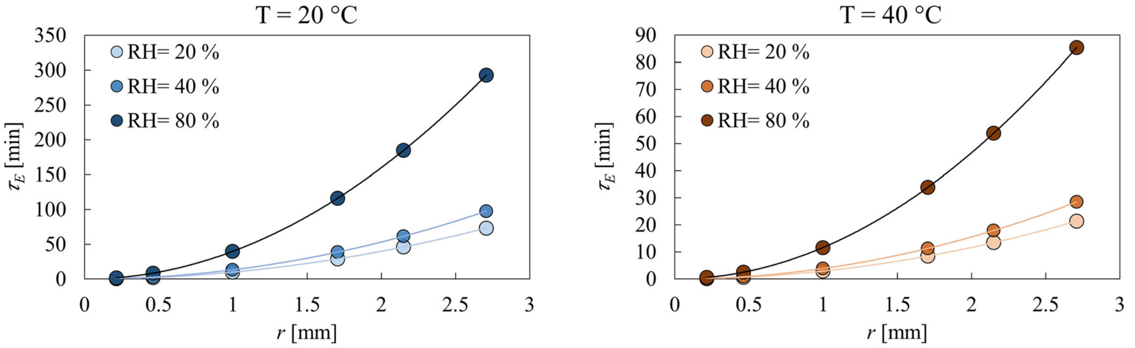

FIG. 22. Sessile droplet (initial contact angle of 60°) evaporation time τ_E chart varying the contact radius and RH with substrate and air temperature of (a) 20 °C and (b) 40 °C.

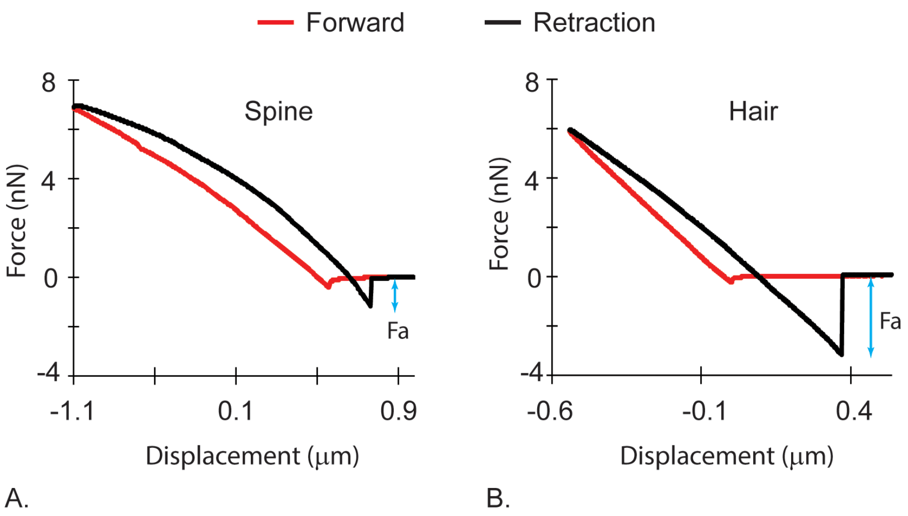

FIG. 23. Representative force-displacement curves from cactus (a) spine and (b) hair.

may infer that the design of the hairs allows for condensation without spreading and further contributes to the partial cooling effect as mentioned above.

All the contact angles experiments showed limitations due to the gripping of the fiber as we have used a double layer adhesive film encapsulating the base of the sample. A second point is that the hairs are not cylindrical but slightly conical; (Table IV) for this reason, the values of the Wilhelmy runs have been analyzed using a mean perimeter value as discussed in the method section.

Finally, Wilhelmy tests were mainly performed in water, but only a few in ethylene glycol and bromonaphthalene have been obtained, with an acceptable behavior (grossly parallel advancing and receding curves in the Wilhelmy plot). However, the results in these last two liquids are not considered as acceptable because they appear higher than the contact angles in water (ethylene glycol: $\vartheta_{adv} = 80°$, $\vartheta_{rec} = 70°$—bromonaphthalene: $\vartheta_{adv}=77°$, $\vartheta_{rec} = 74°$). Quantitatively this is difficult to justify in terms of wettability theory, unless the two liquids interact with the solid surface, possibly modifying the chemistry of the fiber. For this reason, we will not comment on them in terms of acid-base theory. Even in the case of water, this interaction is probably present if one repeats the immersion with the same fiber the contact angle increases, probably because the most hydrophilic part of the surface is released or modified in water (see the re-test values in Table III) and a more hydrophobic layer appears.

To compare the intrinsic wettability of hairs and spines (as they were flat materials without roughness), we first calculated the apparent contact angle (an estimate of the equilibrium contact angle) by using the commonly applied empirical relationship $\vartheta_{apparent,rough} = \cos^{-1}\left[\frac{(\cos\vartheta_{adv}+\cos\vartheta_{rec})}{2}\right]$. Then, by assuming the Wenzel state, we calculated $\vartheta_{app,flat} = \cos^{-1}[(\cos\vartheta_{app})/r_W]$ (Drelich *et al.*, 2020). The dimensionless roughness parameter r_W, also called Wenzel parameter, is obtained from AFM scans (Table II). The assumption of the Wenzel state is justified by the absence of overhangs of the microstructures as seen in SEM images. For spines, $\vartheta_{apparent,rough} = 45.5 \pm 3.3°$ and $\vartheta_{app,flat} = 48.9 \pm 3.2°$, while for hairs see Table III. Comparing $\vartheta_{app,flat}$, spines are more hydrophilic than hairs and even more if the hairs are rewetted. Based on classical nucleation theory (CNT) (Kalikmanov, 2013), we expect that dew nucleation and growth would be more favorable on spines. Experiments in real or controlled environments (radiative cooling chambers) could characterize condensation on the whole plant and better define the role of both structures.

E. Mechanical properties

We measured the mechanical properties of the cactus hairs using tensile tests. The stress-strain curves showed some variations in terms of slope, thus Young's modulus and the values of tensile strength [Fig. 25(a)]. Young's modulus of the cactus hairs was estimated to be 6.1 ± 1.7 GPa. The modulus values are comparable to that of coir (6 GPa) and cotton fibers (6–10 GPa), but the hairs broke at much lower strains in comparison. The tensile strength of the hairs was 209 ± 111 MPa (Table V). The variation in the percentage of breaking strains (2 ± 0.5) was more probably owing to the differences in the hair diameter and its variation along the length. The toughness modulus (area under stress-strain curve) values of cactus hairs (1.88 ± 1.32 $\mathrm{MJ/m^3}$) were on the order of sisal fiber values (4–7.8 $\mathrm{MJ/m^3}$) (Chand and Hashmi, 1993). We measured the ultimate strain (%) of the hairs to be 2 ± 0.5 in tension and that of spines to be 2.2 ± 0.02 in bending. The flexural modulus

TABLE III. Average values of the measured contact angles in the water of the hairs.

Test	Average diameter (μm)	$\vartheta_{advancing}$ (°)	$\vartheta_{receding}$ (°)	$\vartheta_{apparent,rough}$ (°)	$\vartheta_{apparent,flat}$ (°)
Fresh test	28.8 ± 3.1	74 ± 5	59 ± 5	66.7 ± 3.5	70.3 ± 3.2
Re-test		85 ± 4	65 ± 4	75.2 ± 2.8	77.4 ± 2.5

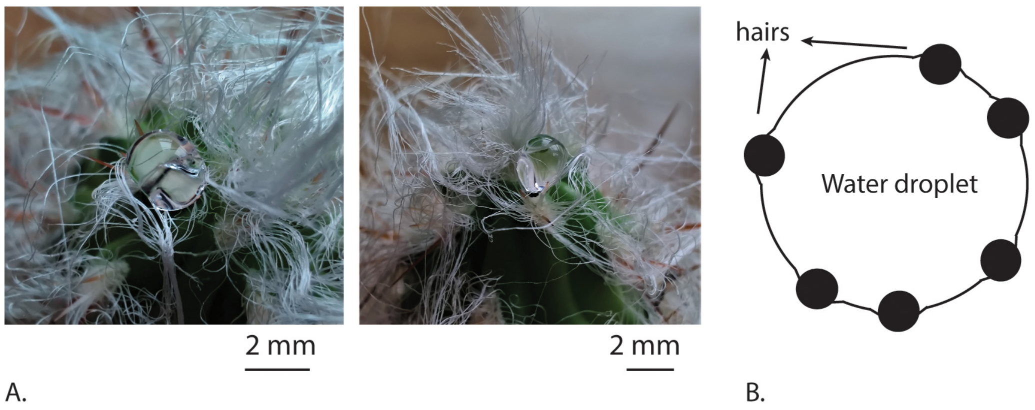

FIG. 24. (a) Images of droplets on the hair sitting hairs. (b) Schematic of the possible droplet-hairs interaction in the plane perpendicular to the hair length.

TABLE IV. Cactus hair dimension measured indirectly from Wilhelmy method.

Cactus hair number	Near base diameter (μm)	Near tip diameter (μm)	Distance of measurement from the tip of the hair (mm)
1	31 ± 1	26 ± 1	7.5
2	70 ± 2	29 ± 1	10.25
3	36 ± 1	35 ± 2	9
4	64 ± 2	16 ± 1	10.3

and flexural strength of the spines were estimated to be 23.9 ± 7.8 and 835 ± 228 MPa, respectively [Fig. 26(b)]. These results show that the spines are nearly 4 times both stiffer and stronger (with a value comparable to high strength steel) compared to the hairs, also in agreement with their suggested role of acting as a physical defence. The observed values of bending strength are much higher compared to 24 species of cactus analyzed in a comparative study where the highest values of bending strength (491 MPa) are reported for *Ferocactus viridescens* (Martinez *et al.*, 2017). The bending strength of *Orocereus trolli* is comparable to the measured values (896 MPa) of dry spines of *Opuntia ficus-indica* (Gindl-Altmutter and Keckes, 2012). The superior mechanical properties of *Optunia ficus-indica* were attributed to high cellulose orientation and high crystallinity of the fiber cells (Gindl-Altmutter and Keckes, 2012). The columnar cacti are visited by many birds because they offer fruits (Godínez-Alvarez *et al.*, 2002). According to nocturnal filming (Munguía-Rosas *et al.*, 2010), 3% of the legitimate visits of the *Pilosocereus leucocephalus* columnar cactus were by large birds (hummingbirds). The high bending modulus and strength of spines may also aid in supporting the weight of the birds and result in less buckling and breakages, in addition to providing physical defence against herbivores, whereas the hairs on the plant surfaces are hypothesized to be a part of the direct defence against insects herbivores (War *et al.*, 2012).

The fractured surface of the hair cross sections confirmed that they contain fiber bundles probably comprised of micro- and

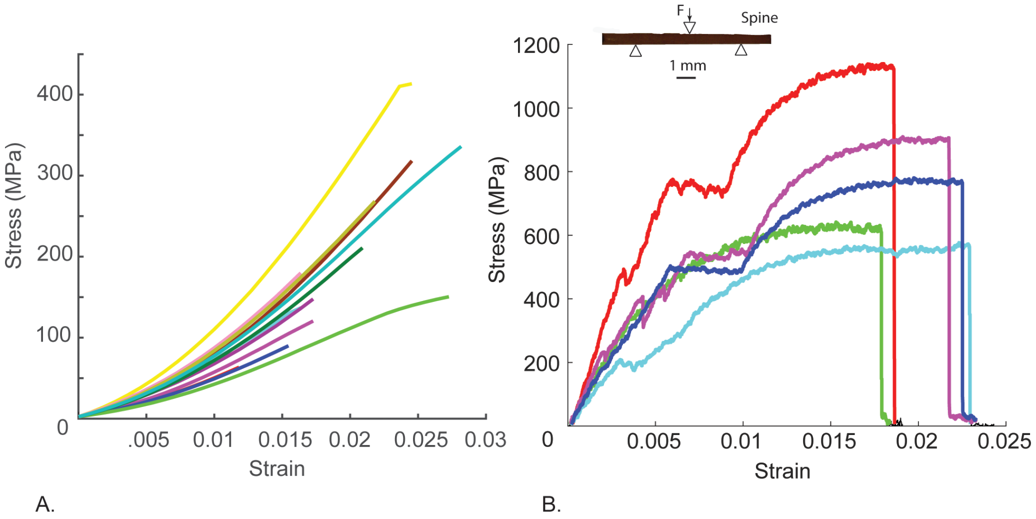

FIG. 25. Stress-strain curves: (a) tensile tests of cactus hairs or (b) bending tests of spines, the inset showing the setup.

TABLE V. Mechanical properties of the cactus hairs (tension) and spines (bending).

Samples	Number	Elastic modulus (GPa)	Fracture strength (MPa)	Toughness modulus (MJ/m^3)	Ultimate strain (%)
Hairs	12	6.1 ± 1.7	209 ± 111	1.88 ± 1.32	2 ± 0.5
Spines	5	23.9 ± 7.8	835 ± 228	11.9 ± 0.3	2.2 ± 0.02

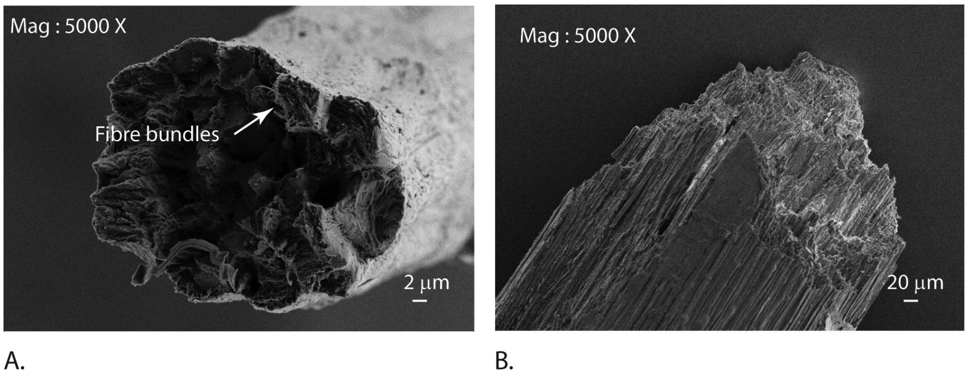

FIG. 26. Scanning electron micrographs: (a) hair cross section after tensile tests and (b) sross section of the spine.

nano-sized components [Fig. 26(a)]. The inner core of the fiber appears to be different from the outer core because of the different nature of the fracture as seen in Fig. 26(a). The fractured surface of the spine showed that it comprises microfibres that are nearly homogeneously packed [Fig. 26(b)].

IV. CONCLUSION

In this work, we investigated the multifunctional role of the appendages of a cactus plant using different approaches. We reported for the first time the phenomenon of *distant coalescence* during condensation on a natural surface and proposed an analytical model to describe it. The model is in good agreement with the experiments in each sub-phase during which the contact radii are constant. The condensate accumulation into a few large drops instead of many smaller ones can speed up the process to achieve critical volume for sliding. Moreover, this can prolong the evaporation time and may aid in maintaining a more stable microclimate among the hairs and in pollination by providing droplets that can attract animals. The general emptying criterion can help in developing novel cactus-inspired materials with engineered contact angle hysteresis for improving water and energy management in dry and hot environments. Mechanical tests revealed that the spines of *Oreocereus trolli* have higher flexural strength than the spines of many cacti species studied earlier and thus ensure greater defence from herbivores and fewer buckling and breakages due to bird visits. Future studies focused on the stick and slip phenomenon during the flux, and on surfaces with a standard channel geometry, will improve the current understanding.

SUPPLEMENTARY MATERIAL

See the supplementary material for additional data from condensation experiments and the derivation of bending stress-strain relationships.

ACKNOWLEDGMENTS

The authors would like to thank Lorenzo Moschini, Professor Devid Maniglio, Professor Antonella Motta, and Professor Claudio Migliaresi (Biotech—Mattarello, University of Trento) for their support with SEM and AFM facility and Evgeny Demenev and Stefano Girardi (Bruno Kessler Foundation, MNF research group, Trento, Italy) for their support in setting up the experimental apparatus for condensation experiments. N.M.P. was supported by the European Commission under the FET Open (Boheme) Grant No. 863179. G.G. was supported by the Caritro Foundation (Prot. U1277.2020/SG.1130). L.K. was supported by the Caritro Foundation (No: 40103264).

AUTHOR DECLARATIONS

Conflict of Interest

The authors have no conflicts to disclose.

Author Contributions

L.K. and N.G.D. contributed equally to this work.

DATA AVAILABILITY

The data that support the findings of this study are available within the article and its supplementary material.

REFERENCES

Abràmoff, M. D., Magalhães, Paulo J., and Ram, Sunanda J. Biophotonics international **11**(7), 36–42 (2004).

Berthier, E., and Beebe, D. J., "Flow rate analysis of a surface tension driven passive micropump," Lab Chip **7**, 1475–1478 (2007).

Bintein, P. B., Lhuissier, H., Mongruel, A., Royon, L., and Beysens, D., "Grooves accelerate dew shedding," Phys. Rev. Lett. **122**, 98005 (2019).

Cao, M., Ju, J., Li, K., Dou, S., Liu, K., and Jiang, L., "Facile and large-scale fabrication of a cactus-inspired continuous fog collector," Adv. Funct. Mater. **24**, 3235–3240 (2014).

Castillo, J. E., Weibel, J. A., and Garimella, S. V., "The effect of relative humidity on dropwise condensation dynamics," Biol. Control **80**, 759–766 (2015).

Chand, N., and Hashmi, S. A. R., "Mechanical properties of sisal fibre at elevated temperatures," J. Mater. Sci. **28**, 6724–6728 (1993).

Chen, H., Ran, T., Gan, Y., Zhou, J., Zhang, Y., Zhang, L. *et al.*, "Ultrafast water harvesting and transport in hierarchical microchannels," Nat. Mater **17**, 935–942 (2018).

Chu, F., Wu, X., Zhu, Y., and Yuan, Z., "Relationship between condensed droplet coalescence and surface wettability," Int. J. Heat Mass Transfer **111**, 836–841 (2017).

Della Volpe, C., Siboni, S., Maniglio, D., and Morra, M., "An experimental procedure to obtain the equilibrium contact angle from the Wilhelmy method. BT—Wetting and spreading: From microscopic origins to industrial processes," Oil Gas Sci. Technol. **56**, 9–22 (2001).

Drelich, J. W., Boinovich, L., Chibowski, E., Della Volpe, C., Hołysz, L., Marmur, A. *et al.*, "Contact angles: History of over 200 years of open questions," Surf. Innovations **8**, 3–27 (2020).

Ehleringer, J., and Mooney, H., "Leaf hairs: Efeects on physiologyical activity and adaptive value to a desert shrub," Oecologia **37**, 183–125 (1978).

Farner, D. S., King, J. R., and Parkes, K. C., Avian Biology (New York and London: Academic Press, 1970), Vol. I. pp. 586.

Freeman, B. C., and Beattie, G. A., "An overview of plant defenses against pathogens and herbivores," Plant Health. Instr. (online, 2008); available at https://dr.lib.iastate.edu/entities/publication/27a4e983-bebc-4150-acac-d322ca26a53b.

Gindl-Altmutter, W., and Keckes, J., "The structure and mechanical properties of spines from the cactus Opuntia ficus-indica," BioResources **7**, 1232–1237 (2012).

Godínez-Alvarez, H., Valiente-Banuet, A., and Rojas-Martínez, A., "The role of seed dispersers in the population dynamics of the columnar cactus Neobuxbaumia tetetzo," Ecology **83**, 2617–2629 (2002).

Gurera, D., and Bhushan, B., "Passive water harvesting by desert plants and animals: Lessons from nature," Philos. Trans. R. Soc. A **378**, 20190444 (2020).

Hanley, M. E., Lamont, B. B., Fairbanks, M. M., and Rafferty, C. M., "Plant structural traits and their role in anti-herbivore defence," Perspect. Plant Ecol. Evol. Syst. **8**, 157–178 (2007).

Hou, K., Li, X., Li, Q., and Chen, X., "Tunable wetting patterns on superhydrophilic/superhydrophobic hybrid surfaces for enhanced dew-harvesting efficacy," Adv. Mater. Interfaces **7**, 1901683 (2020).

Hu, H., and Larson, R. G., "Evaporation of a sessile droplet on a substrate," J. Phys. Chem. B **106**, 1334–1344 (2002).

Huhtamäki, T., Tian, X., Korhonen, J. T., and Ras, R. H. A., "Surface-wetting characterization using contact-angle measurements," Nat. Protoc. **13**, 1521–1538 (2018).

Jia, Z., Zhao, Z., Zhang, Q., and Wu, W., "Dew yield and its influencing factors at the western edge of Gurbantunggut Desert, China," Water **11**, 733 (2019).

Jones, H. G., and Rotenberg, E., "Energy, radiation and temperature regulation in plants," eLs **2001**, 1–7.

Ju, J., Bai, H., Zheng, Y., Zhao, T., Fang, R., and Jiang, L., "A multi-structural and multi-functional integrated fog collection system in cactus," Nat. Commun **3**, 1246–1247 (2012).

Kalikmanov, V. I., "Nucleation theory," Lect. Notes Phys. **860**, 1–331 (2013).

Keeley, J. E., and Keeley, S. C., "Crassulacean acid metabolism (CAM) in high elevation tropical cactus," Plant. Cell Environ. **12**, 331–336 (1989).

Koch, K., Bhushan, B., and Barthlott, W., "Multifunctional surface structures of plants: An inspiration for biomimetics," Prog. Mater. Sci. **54**, 137–178 (2009).

Lee, A., Moon, M. W., Lim, H., Kim, W. D., and Kim, H. Y., "Water harvest via dewing," Langmuir **28**, 10183–10191 (2012).

Lendel, A., *South American Cacti in Time and Space: Studies on the Diversification of the Tribe Cereeae, with Particular Focus on Subtribe Trichocereinae (Cactaceae)* thesis (University of Zurich, Faculty of Science, 2013), Vol. 285.

Lewis, D. A., and Nobel, P. S., "Thermal energy exchange model and water loss of a barrel cactus, ferocactus acanthodes," Plant Physiol. **60**, 609–616 (1977).

Li, C., Yu, C., Zhou, S., Dong, Z., and Jiang, L., "Liquid harvesting and transport on multiscaled curvatures," Proc. Natl. Acad. Sci. U. S. A. **117**, 23436–23442 (2020).

Liu, C., Xue, Y., Chen, Y., and Zheng, Y., "Effective directional self-gathering of drops on spine of cactus with splayed capillary arrays," Sci. Rep. **5**, 1–8 (2015).

Malik, F. T., Clement, R. M., Gethin, D. T., Kiernan, M., Goral, T., Griffiths, P. *et al.*, "Hierarchical structures of cactus spines that aid in the directional movement of dew droplets," Philos. Trans. R. Soc. A **374**, 20160110 (2016).

Malik, F. T., Clement, R. M., Gethin, D. T., Krawszik, W., and Parker, A. R., "Nature's moisture harvesters: A comparative review," Bioinspiration Biomimetics **9**, 031002 (2014).

Martinez, J., Stewart, T., and Szeto, P., "The relationship between structural parameters and mechanical properties of cactus spines," thesis (2017), available at https://digitalcommons.calpoly.edu/cgi/viewcontent.cgi?article=1171&context=matesp.

Masrahi, Y. S., "Glochids microstructure and dew harvesting ability in *Opuntia stricta* (Cactaceae)," J. King Saud Univ.- Sci. **32**, 3307–3312 (2020).

Melin, J., Van Der Wijngaart, W., and Stemme, G., "Behaviour and design considerations for continuous flow closed-open-closed liquid microchannels," Lab Chip **5**, 682–686 (2005).

Munguía-Rosas, M. A., Sosa, V. J., and Jácome-Flores, M. E., "Pollination system of the Pilosocereus leucocephalus columnar cactus (tribe Cereeae) in eastern Mexico," Plant Biol. **12**, 578–586 (2010).

Narhe, R., Beysens, D., and Nikolayev, V. S., "Contact line dynamics in drop coalescence and spreading," Langmuir **20**, 1213–1221 (2004).

Orejon, D., Sefiane, K., and Shanahan, M. E. R., "Stick-slip of evaporating droplets: Substrate hydrophobicity and nanoparticle concentration," Langmuir **27**, 12834–12843 (2011).

Pan, Z., Pitt, W. G., Zhang, Y., Wu, N., Tao, Y., and Truscott, T. T., "The upside-down water collection system of *Syntrichia caninervis*," Nat. Plants **2**, 1–5 (2016).

Park, S. N., *Cacti: Biology and Uses* (University of California Press, 2002).

Roth-Nebelsick, A., Ebner, M., Miranda, T., Gottschalk, V., Voigt, D., Gorb, S. *et al.*, "Leaf surface structures enable the endemic Namib desert grass Stipagrostis sabulicola to irrigate itself with fog water," J. R. Soc. Interface **9**, 1965–1974 (2012).

Schlegel, U., "The composite structure of cactus spines," Bradleya **27**, 129–138 (2009).

Seemann, R., Brinkmann, M., Kramer, E. J., Lange, F. F., and Lipowsky, R., "Wetting morphologies at microstructured surfaces," Proc. Natl. Acad. Sci. U. S. A. **102**, 1848–1852 (2005)..

Sharma, C. S., Lam, C. W. E., Milionis, A., Eghlidi, H., and Poulikakos, D., "Self-sustained cascading coalescence in surface condensation," ACS Appl. Mater. Interfaces **11**, 27435–27442 (2019).

Shawki, M. A.-A., Titěra, D., Kazda, J., Kohoutková, J., and Táborský, V., "Toxicity to honeybees of water guttation and dew collected from winter rape treated with Nurelle D$^{®}$," Plant Protection Science **42**, 9–14 (2006).

Shi, N. N., Tsai, C. C., Camino, F., Bernard, G. D., Yu, N., and Wehner, R., "Keeping cool: Enhanced optical reflection and radiative heat dissipation in Saharan silver ants," Science **349**, 298–301 (2015).

Shirtcliffe, N. J., McHale, G., and Newton, M. I., "Learning from superhydrophobic plants: The use of hydrophilic areas on superhydrophobic surfaces for droplet control," Langmuir **25**, 14121–14128 (2009).

Trosseille, J., Mongruel, A., Royon, L., and Beysens, D., "Radiative cooling for dew condensation," Int. J. Heat Mass Transfer **172**, 121160 (2021).

War, A. R., Paulraj, M. G., Ahmad, T., Buhroo, A. A., Hussain, B., Ignacimuthu, S. *et al.*, "Mechanisms of plant defense against insect herbivores," Plant Signal. Behav. **7**, 1306–1320 (2012).

Yang, J., Yang, Z., Chen, C., and Yao, D., "Conversion of surface energy and manipulation of a single droplet across micropatterned surfaces," Langmuir **24**(17), 9889–9897 (2008).

Zhang, L., Liu, G., Chen, H., Liu, X., Ran, T., Zhang, Y. *et al.*, "Bioinspired unidirectional liquid transport micro-nano structures: A review," J. Bionic Eng. **18**, 1–29 (2021).

Zhang, Q., Wang, S., Yang, F. L., Yue, P., Yao, T., and Wang, W. Y., "Characteristics of dew formation and distribution, and its contribution to the surface water budget in a semi-arid region in China," Boundary-Layer Meteorol **154**, 317–331 (2015).

Zhu, F., Fang, W. Z., Zhang, H., Zhu, Z., New, T. H., Zhao, Y. *et al.*, "Water condensate morphologies on a cantilevered microfiber," J. Appl. Phys **127**, 244902 (2020).

Supplementary Material

Multifunctional roles of hairs and spines in Old Man of the Andes Cactus: droplet distant coalescence, and mechanical strength

Lakshminath Kundanati[1,†], Nicolò G. Di Novo[1,2,†], Gabriele Greco[1], Stefano Siboni[3], Claudio della Volpe[3], Alvise Bagolini[2], Nicola M. Pugno[1,4,*]

[1] *Laboratory for Bioinspired, Bionic, Nano, Meta, Materials & Mechanics, Department of Civil, Environmental and Mechanical Engineering, University of Trento, Via Mesiano, 77, 38123 Trento, Italy*

[2] *Center for Materials and Microsystems, FBK, Via Sommarive 18, 38123 Trento*

[3] *Department of Civil, Environmental and Mechanical Engineering, University of Trento, Trento, Italy*

[4] *School of Engineering and Materials Science, Queen Mary University of London, Mile End Road, London E1 4NS, United Kingdom*

[†] *These authors contributed equally to this work*

**corresponding author: nicola.pugno@unitn.it*

Content

- **S1**: As a support to Fig. 13, in Fig. S1.1 we report the measured heights and contact radii and calculated longitudinal curvature radii and contact angles of the distant coalescence events Exp 1.1, Exp 1.2, Exp 1.2, Exp 2.1, Exp 2.2, Exp 3.1 and Exp 3.2. In Figure S1.2 we report the comparison between measured and simulated heights of the distant coalescence events Exp 1.1, Exp 1.2, Exp 2.2, Exp 3.1 and Exp 3.2.
- **S2**: Derivation of stress-strain relationships for conical beam in bending
- **S3**: Schematic of the experimental setup for the condensation experiments
- **S4**: Water bridge formation between the spine and the plate in condensation experiments in configuration 1
- **S5**: Parameters L,W and contact radii of each flow phase used in the calculations.

S1.1 Evolution of the measured heights and contact radii and calculated curvature radii and contact angles.

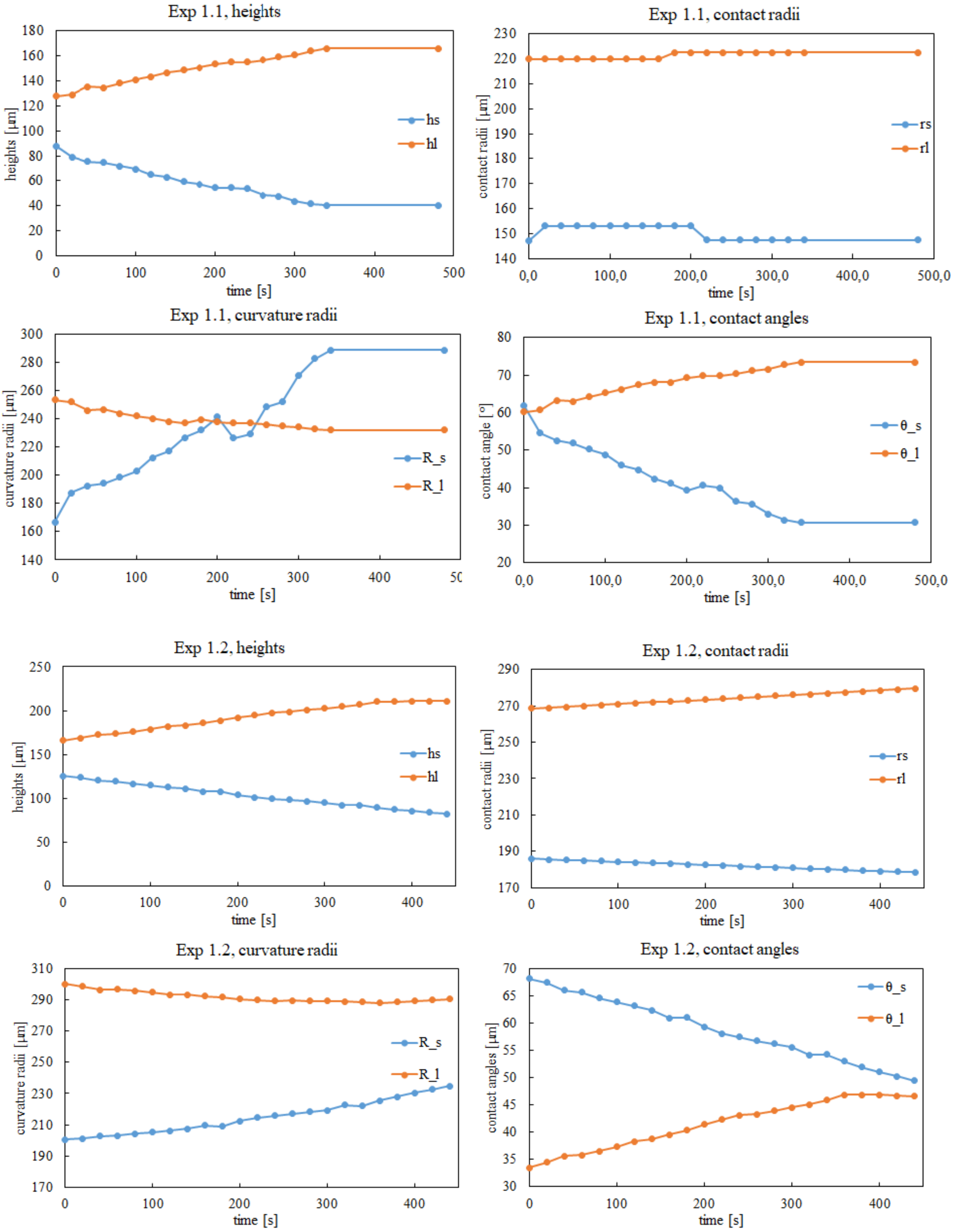

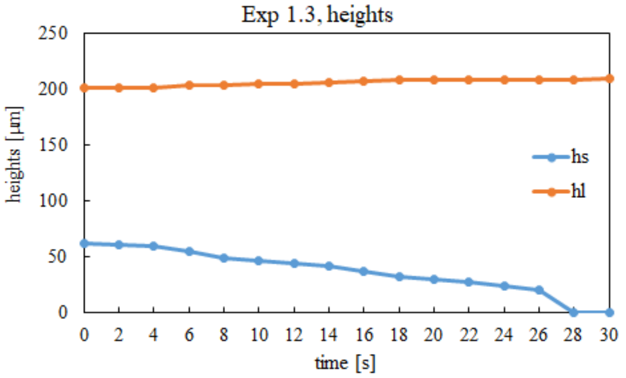
Exp 1.3, heights
heights [μm]
250
200
150
100
50
0
0 2 4 6 8 10 12 14 16 18 20 22 24 26 28 30
time [s]
hs
hl

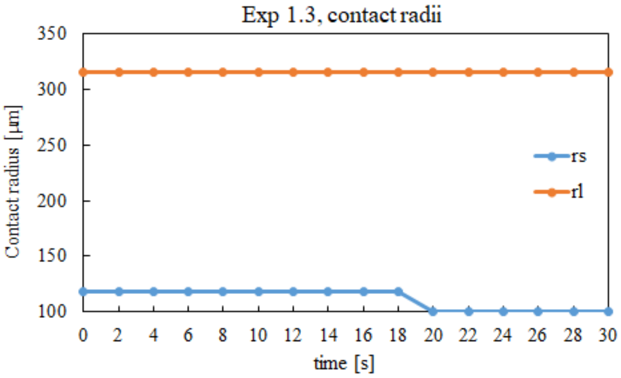
Exp 1.3, contact radii
Contact radius [μm]
350
300
250
200
150
100
0 2 4 6 8 10 12 14 16 18 20 22 24 26 28 30
time [s]
rs
rl

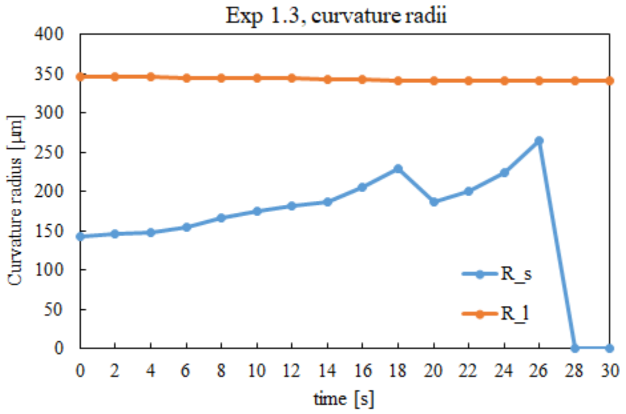
Exp 1.3, curvature radii
Curvature radius [μm]
400
350
300
250
200
150
100
50
0
0 2 4 6 8 10 12 14 16 18 20 22 24 26 28 30
time [s]
R_s
R_l

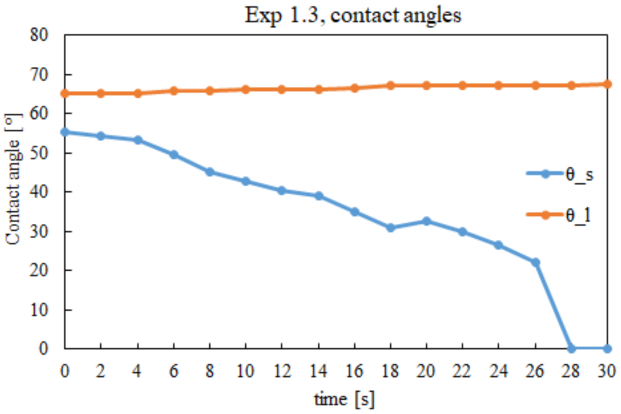
Exp 1.3, contact angles
Contact angle [°]
80
70
60
50
40
30
20
10
0
0 2 4 6 8 10 12 14 16 18 20 22 24 26 28 30
time [s]
θ_s
θ_l

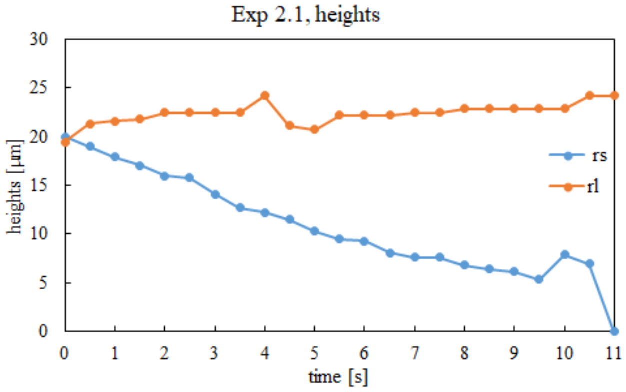
Exp 2.1, heights
heights [μm]
30
25
20
15
10
5
0
0 1 2 3 4 5 6 7 8 9 10 11
time [s]
rs
rl

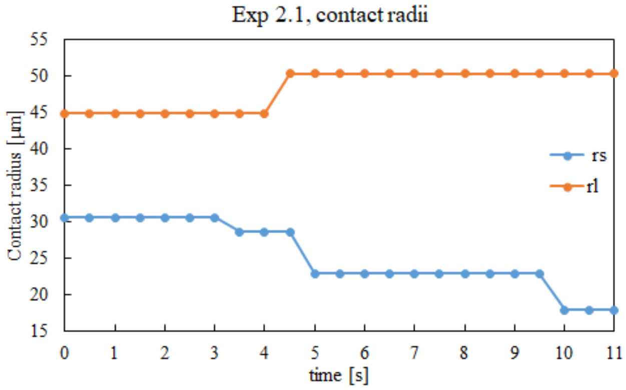
Exp 2.1, contact radii
Contact radius [μm]
55
50
45
40
35
30
25
20
15
0 1 2 3 4 5 6 7 8 9 10 11
time [s]
rs
rl

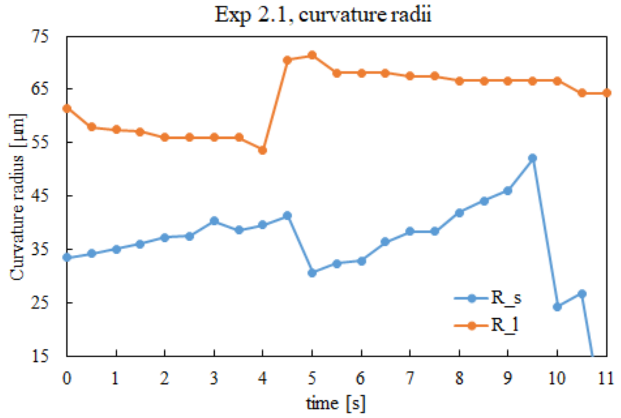
Exp 2.1, curvature radii
Curvature radius [μm]
75
65
55
45
35
25
15
0 1 2 3 4 5 6 7 8 9 10 11
time [s]
R_s
R_l

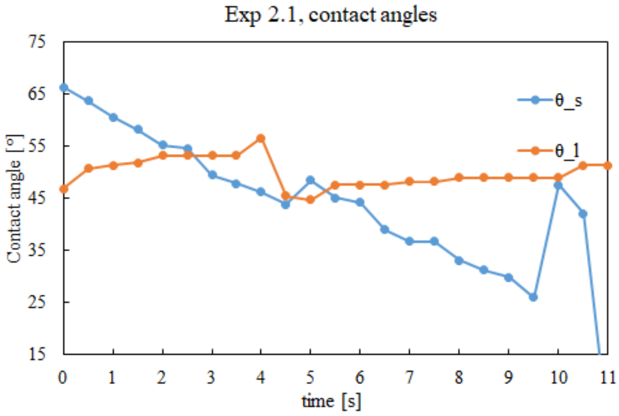
Exp 2.1, contact angles
Contact angle [°]
75
65
55
45
35
25
15
0 1 2 3 4 5 6 7 8 9 10 11
time [s]
θ_s
θ_l

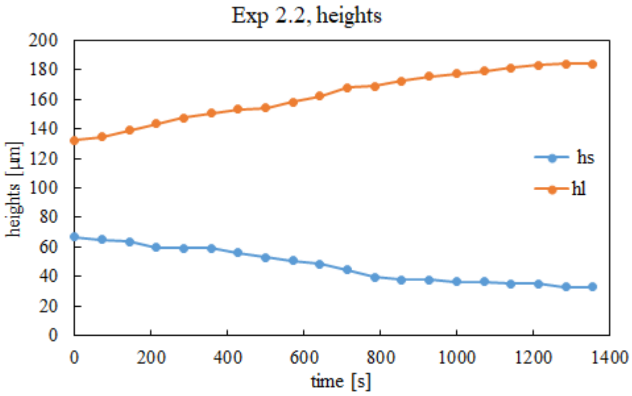
Exp 2.2, heights
heights [µm]
0
20
40
60
80
100
120
140
160
180
200
0
200
400
600
800
1000
1200
1400
time [s]
hs
hl

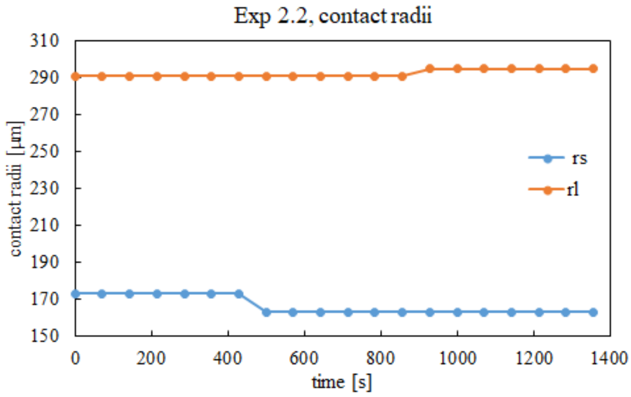
Exp 2.2, contact radii
contact radii [µm]
150
170
190
210
230
250
270
290
310
0
200
400
600
800
1000
1200
1400
time [s]
rs
rl

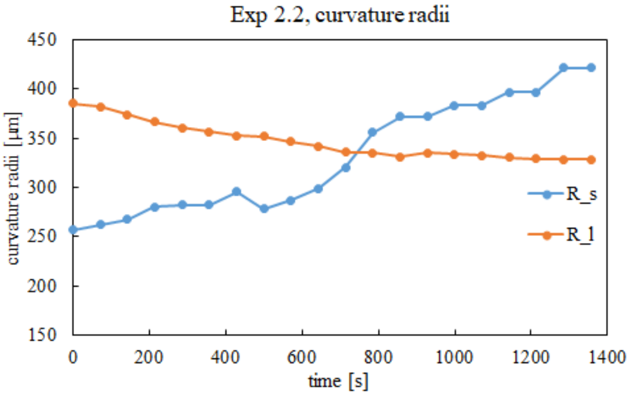
Exp 2.2, curvature radii
curvature radii [µm]
150
200
250
300
350
400
450
0
200
400
600
800
1000
1200
1400
time [s]
R_s
R_1

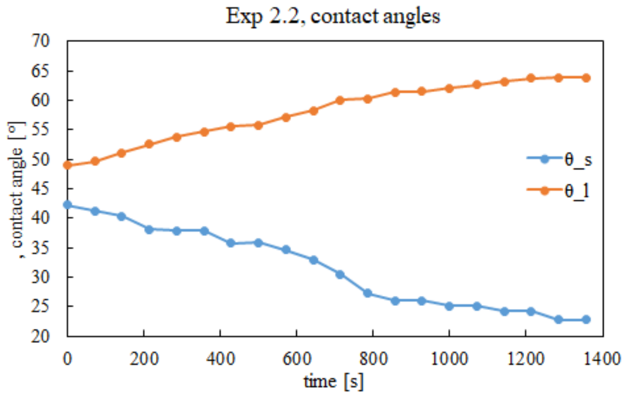
Exp 2.2, contact angles
, contact angle [°]
20
25
30
35
40
45
50
55
60
65
70
0
200
400
600
800
1000
1200
1400
time [s]
θ_s
θ_1

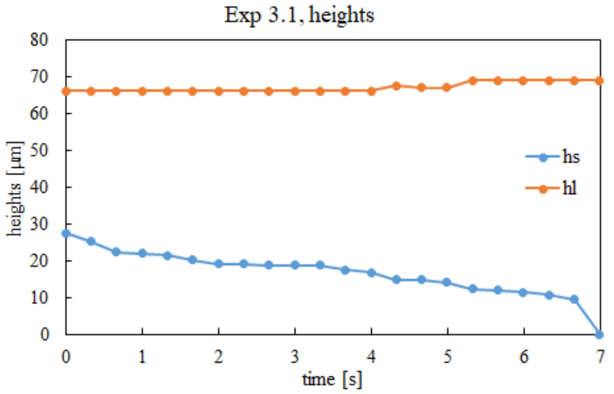
Exp 3.1, heights
heights [µm]
0
10
20
30
40
50
60
70
80
0
1
2
3
4
5
6
7
time [s]
hs
hl

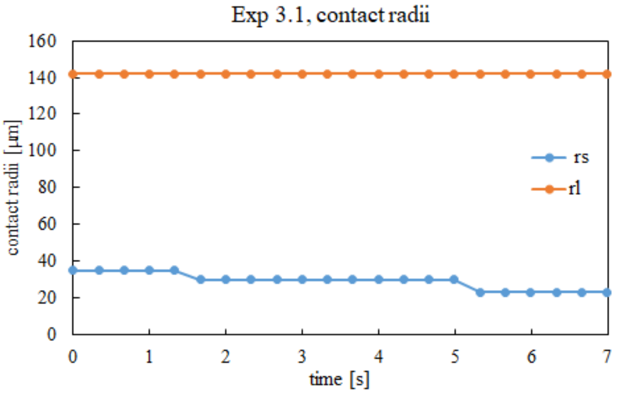
Exp 3.1, contact radii
contact radii [µm]
0
20
40
60
80
100
120
140
160
0
1
2
3
4
5
6
7
time [s]
rs
rl

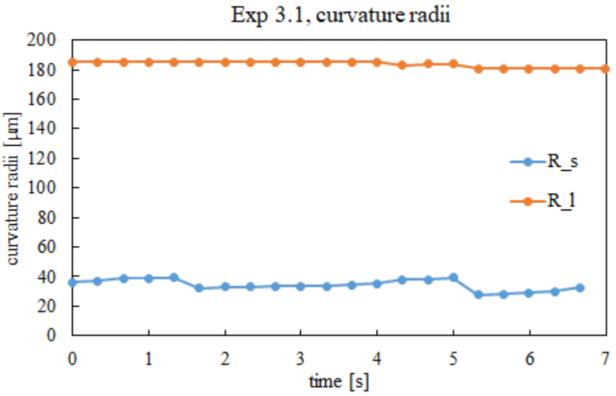
Exp 3.1, curvature radii
curvature radii [µm]
0
20
40
60
80
100
120
140
160
180
200
0
1
2
3
4
5
6
7
time [s]
R_s
R_1

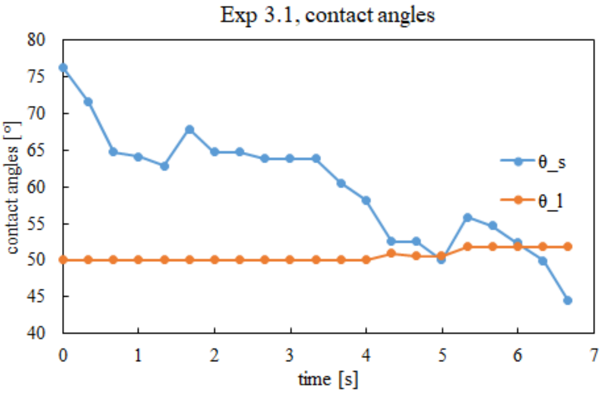
Exp 3.1, contact angles
contact angles [°]
40
45
50
55
60
65
70
75
80
0
1
2
3
4
5
6
7
time [s]
θ_s
θ_1

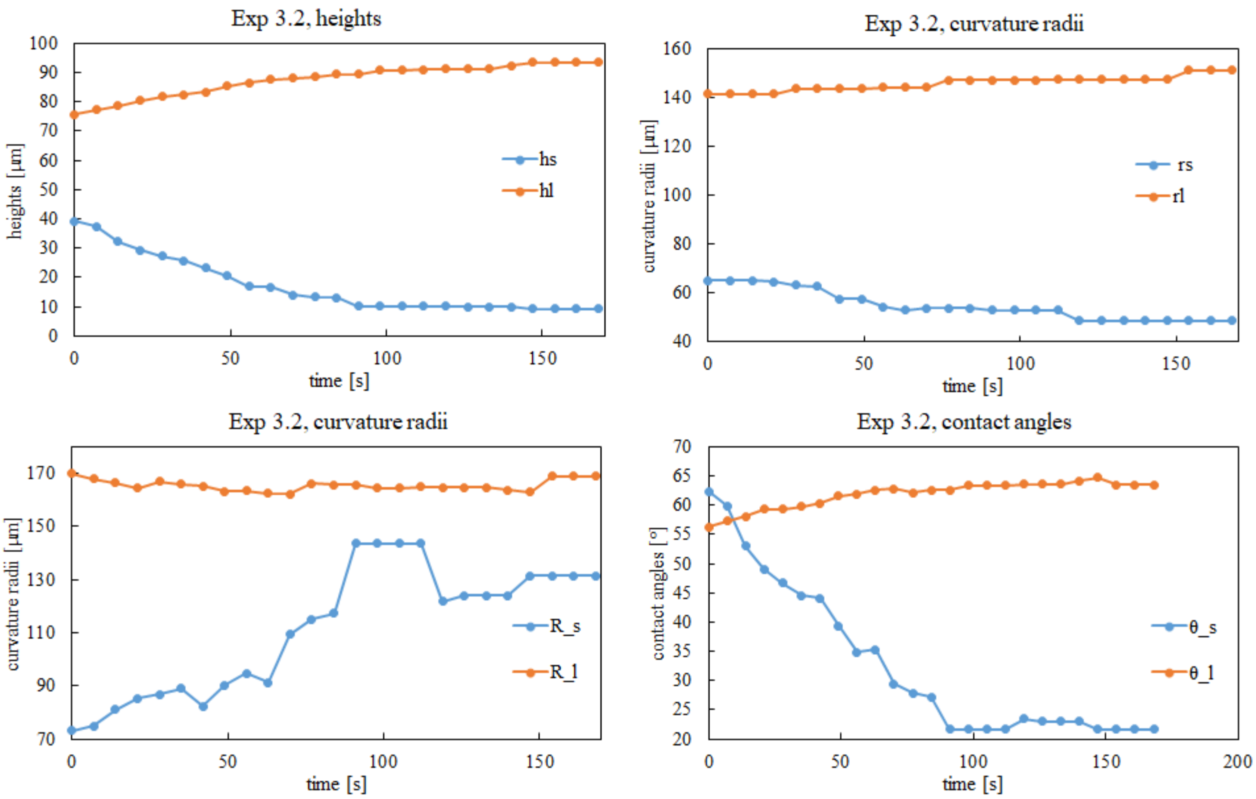

Fig. S1.2 Comparison between measured and simulated heights of the distant coalescence events Exp 1.1, Exp 1.2, Exp 2.2, Exp 3.1 and Exp 3.2.

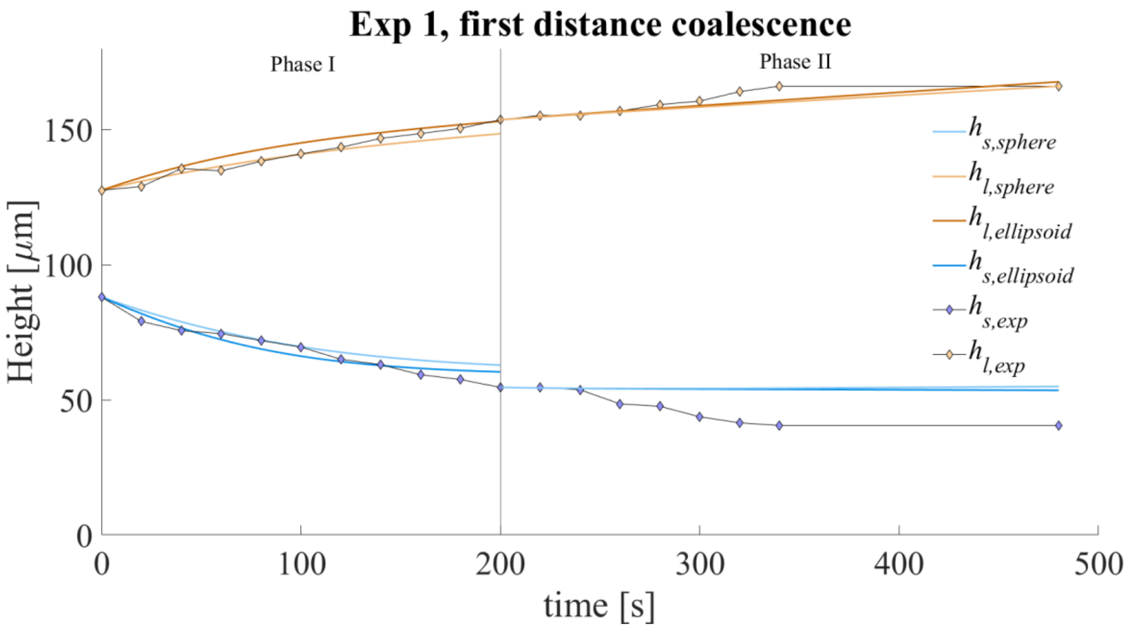

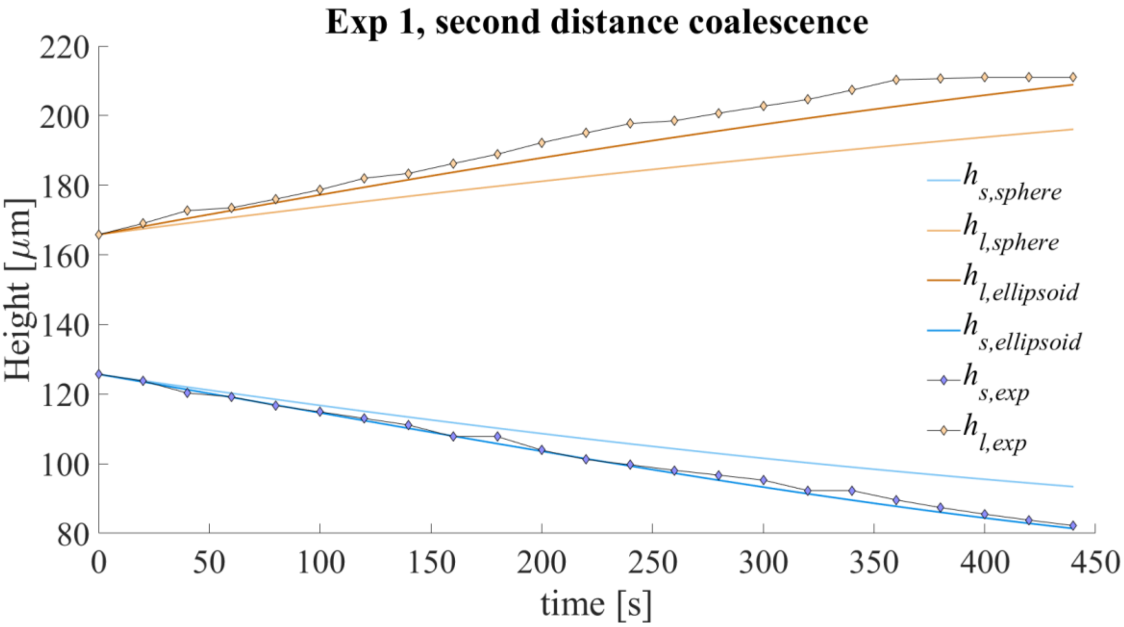

Exp 1, second distance coalescence

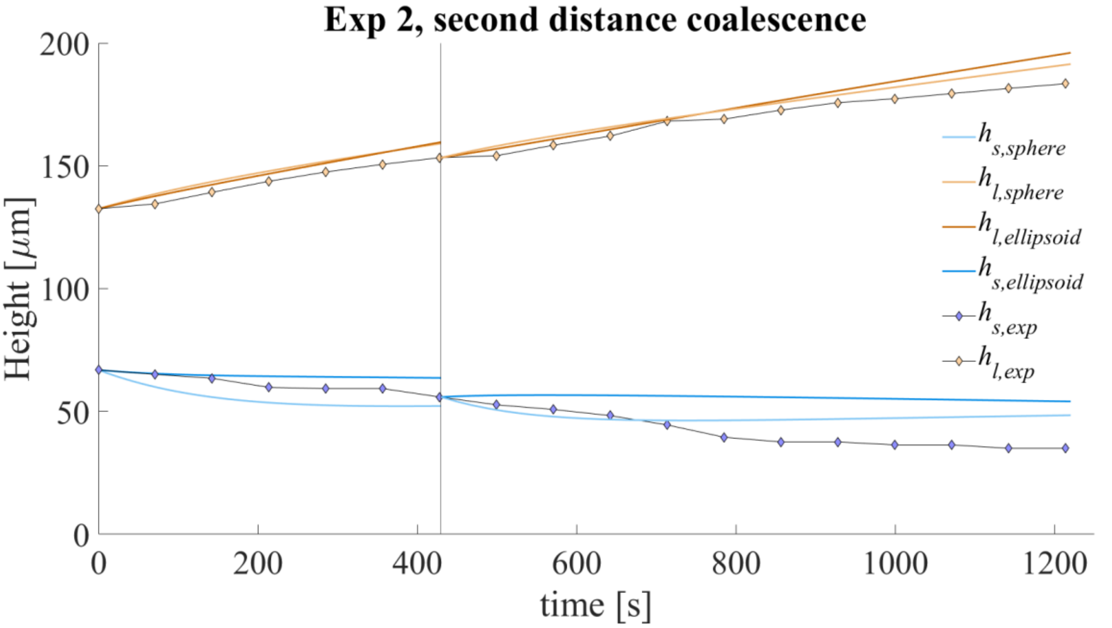

Exp 2, second distance coalescence

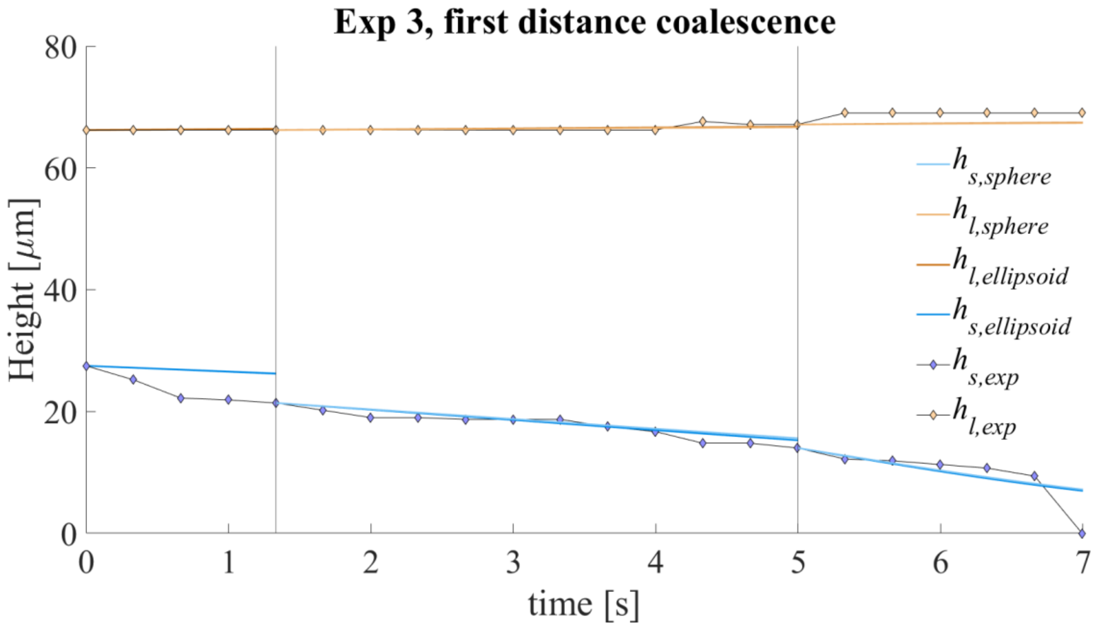
Exp 3, first distance coalescence
Height [μm]
80
60
40
20
0
time [s]
0
1
2
3
4
5
6
7
$h_{s,sphere}$
$h_{l,sphere}$
$h_{l,ellipsoid}$
$h_{s,ellipsoid}$
$h_{s,exp}$
$h_{l,exp}$

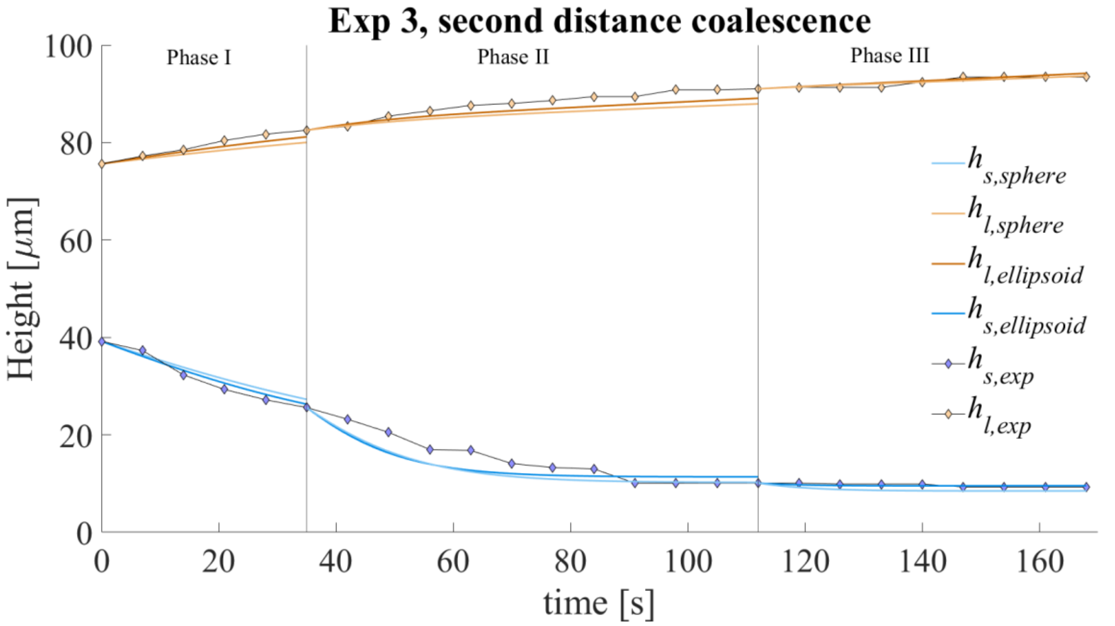
Exp 3, second distance coalescence
Phase I
Phase II
Phase III
Height [μm]
100
80
60
40
20
0
time [s]
0
20
40
60
80
100
120
140
160
$h_{s,sphere}$
$h_{l,sphere}$
$h_{l,ellipsoid}$
$h_{s,ellipsoid}$
$h_{s,exp}$
$h_{l,exp}$

Table S5. Parameters *L*,*W* and contact radii of each flow phase used in the calculations.

Event	*L* (μm)	*W* (μm)	$r_{s,0}$ (μm)	$r_{l,0}$ (μm)
Exp 1.1 phase I	17	14	153	220
Exp 1.1 phase II	17	14	147	223
Exp 1.2	34.5	14	178	279
Exp 1.3, phase I	40	21	122	316
Exp 1.3, phase II	40	21	110	316
Exp 2.1 phase I	8	5.7	31	45
Exp 2.1 phase II	8	5.7	23	50
Exp 2.2 Phase I	28	15	173	291
Exp 2.2 Phase II	28	15	163	295
Exp 3.1 phase I	18	5	35	142
Exp 3.1 phase II	18	5	30	142
Exp 3.1 phase III	18	5	23	142
Exp 3.2 phase I	7	5.7	65	141
Exp 3.2 phase II	7	5.7	53	147
Exp 3.2 phase III	7	5.7	49	151
Exp 3.3, phase I	70	17	170	258
Exp 3.3, phase II	70	17	150	266
Exp 3.3, phase III	70	17	125	266

S2: Derivation of stress-strain relationships for conical beam in bending

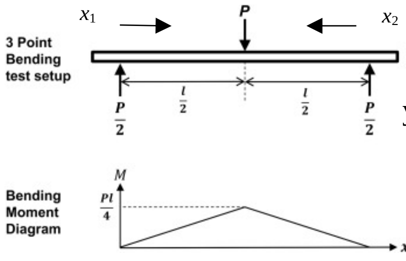

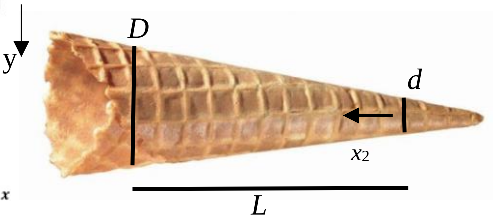

$$conicity\ c = \frac{D-d}{L}$$

For a circular beam of radius *r* the moment of inertia along the bending axis *z* is

$$I_z = \frac{\pi(2r)^4}{64}$$

For a conical beam the radius varies linearly with $x_{1,2}$. Starting from x_2 we can write the diameter as a function of x_2:

$$2r(x_2) = d + c\, x_2$$

while starting from x_1

$$2r(x_1) = D - c\, x_1$$

The bending moment M_z is linear and with a discontinuous derivative (shear) in the centre, where the force P is applied; let's write the stresses starting from both the ends. In general:

$$\sigma_{tensile,fibers\ below} = \frac{M_z y}{I_z}$$

From the right (x_2), the maximum stress at a certain x_2 , by placing $y = r$, is:

$$\sigma_{x2} = \frac{16\, P\, x_2}{\pi(d + c\, x_2)^3}$$

This function is valid for $0 \le x_2 \le \frac{L}{2}$ and may have a maximum in this part of the beam. Imposing the derivative = 0 the max is found in correspondence of

$$x_{2,max} = \frac{d}{2c}$$

which is valid only if

$$0 \le x_{2,max} \le \frac{L}{2}$$

(otherwise the maximum is calculated to be located beyond the middle point, not consider since located out of the validity domain $0 \le x_2 \le \frac{L}{2}$. Therefore, if

$$x_{2,max} > \frac{L}{2}$$

the function in the left half of the beam is an increasing function and it has not a max before the middle of the beam. Since it is an increasing function, the max limited in this part of the beam is in the middle.

Indeed, starting from the left end (x_1) and for $0 \le x_1 \le \frac{L}{2}$ we have similarly:

$$\sigma_{x1} = \frac{16\, P\, x_1}{\pi(D - c\, x_1)^3}$$

For $0 \le x_1 \le \frac{L}{2}$ (zone of interest) this function is increasing and without derivative = 0 (which is for completeness at $x_{1,max} = -\frac{D}{2c}$, a non-physical solution). So, in this half of the beam it grows and reach its higher value in the middle which corresponds to the σ_{x2}. Indeed, the two functions have always the same value in the middle (verified). Thus, the σ_x function is continuous in the middle with non-continuous derivative (verified).

If $0 < x_{2,max} \le \frac{L}{2}$ the maximum stress is therefore at $x_{2,max} = \frac{d}{2c}$ and is:

$$\sigma_{x2,max} = \frac{64\,P}{27\pi\,c\,d^2}$$

If $x_{2,max} > \frac{L}{2}$ the maximum in thus at $x_{max} = \frac{L}{2}$ and is:

$$\sigma_{\frac{L}{2},max} = \frac{64\,P\,L}{\pi\,(2d + c\,L)^3}$$

Interesting to note that for c→0 , $x_{2,max} > \frac{L}{2}$; thus, $\sigma_{max} = \sigma_{\frac{L}{2},max}$, the common values for the constant cross-section beam.

In our case of the spine the conicity is small (from photos c=0.032) and thus the max is in the middle.

Displacement and strain

The vertical displacement function is the following, with E the Young's modulus:

$$v(x_2) = \frac{4\,P}{3\pi E}\frac{x_2(4{x_2}^2 - 3L^2)}{(d + c\,x_2)^4}$$

The maximum displacement δ_{max} is always in the middle at $x_2 = L/2$ (verified by dv/dx=0).

$$\delta_{max} = \frac{64\,P\,L^3}{3\pi E\,(2d + cL)^4}$$

Thus, since in the experiments we measure δ_{max} in the middle, the Young's modulus is the following:

$$E = \frac{64\,P\,L^3}{3\pi\,\delta_{max}\,(2d + cL)^4} \equiv \frac{64\,P\,L^3}{3\pi\,\delta_{max}\,(D + d)^4}$$

Now, having E we can calculate the tensile strain in the axial direction *x*.

$$\varepsilon_{x2} = \frac{\sigma_{x2}}{E} = \frac{M_z y}{E\,I_z}$$

This function has the expression:

$$\varepsilon_{x2} = \frac{16\,P\,x_2}{E\,\pi(d + c\,x_2)^3}$$

A part from the constant *E*, this function is the same of the stress and all the considerations about the maximum and trends are the same.

Therefore, if

$$x_{2,max} = \frac{d}{2c} < \frac{L}{2}$$

the max of the strain (and stress) is located at $x_{2,max} = \frac{d}{2c}$ and is

$$\varepsilon_{x2,max}(\frac{d}{2c}) = \frac{64\,P}{27\pi\,E\,c\,d^2} \equiv \delta_{max}\frac{(2d + c\,L)^4}{9\,c\,d^2 L^3}$$

Alternatively, if

$$x_{2,max} = \frac{d}{2c} > \frac{L}{2}$$

the max of the strain (and stress) is located in the middle at $x_{2,max} = \frac{L}{2}$ and is:

$$\varepsilon_{x2,max}(\frac{L}{2}) = \delta_{max}\frac{3(2d + c\,L)}{L^2}$$

S3: Schematic of the experimental setup for the condensation experiments

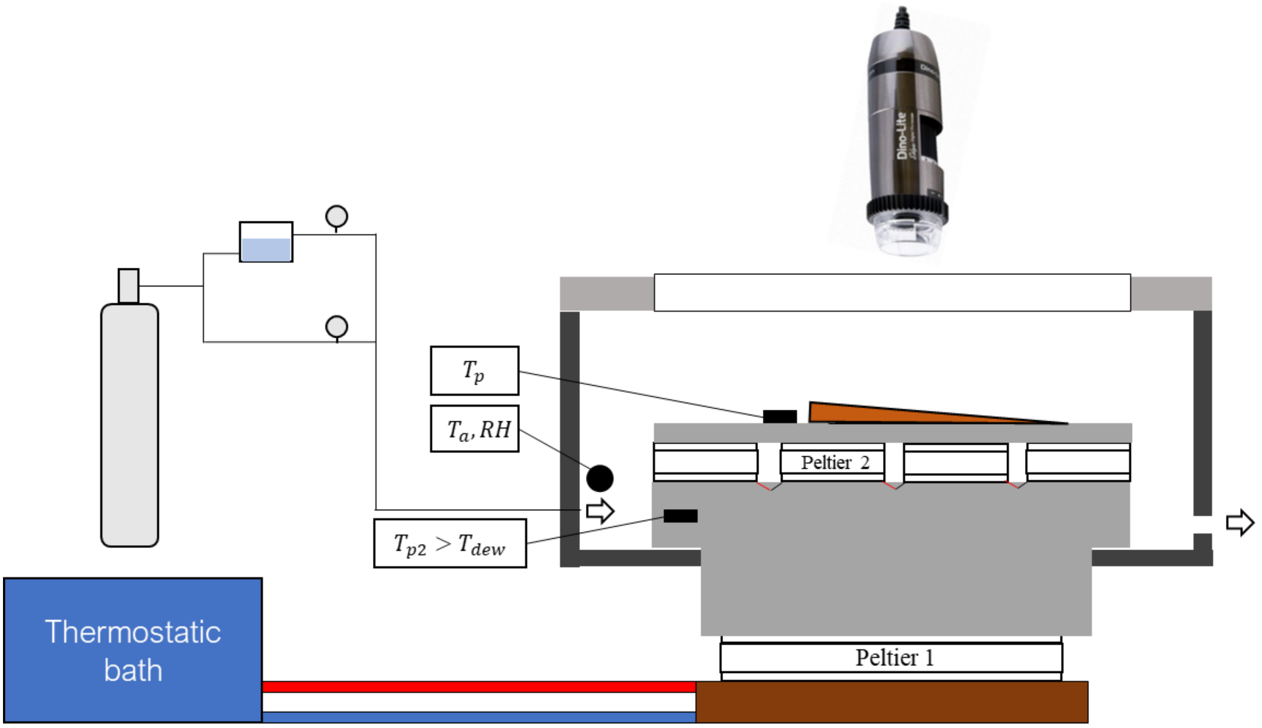

S4: Water bridge formation between the spine and the plate in condensation experiments in configuration 1.

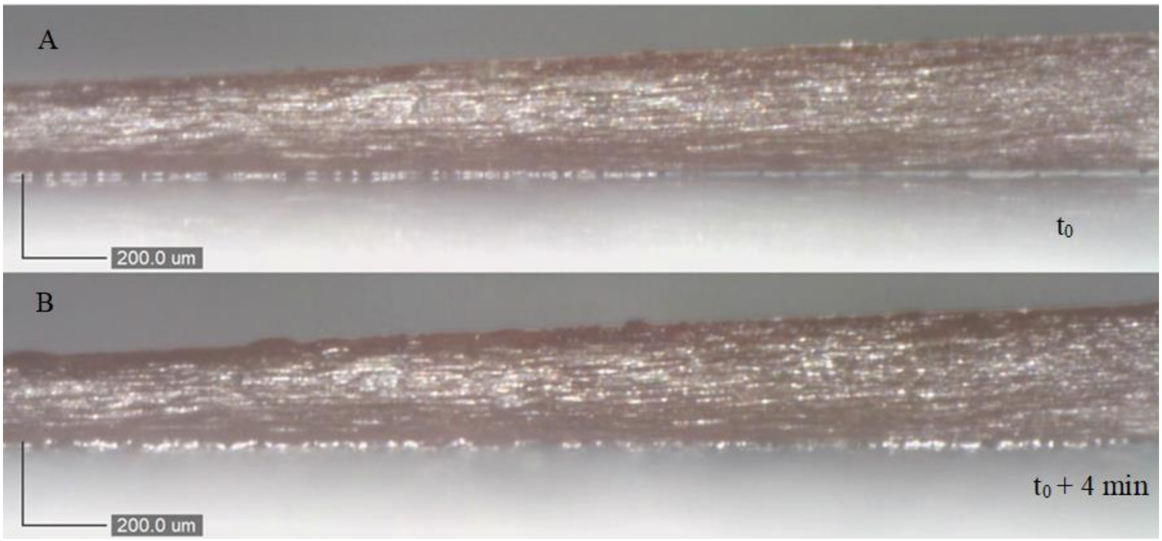

Figure S4. Condensation experiments of a spine in configuration 1. $t_0{\sim}4$ *min. It is clear the formation of a liquid bridge between the spine and the aluminum plate which assures a good and homogeneous thermal contact.*

In the experiments in configuration 1, we observed a complete formation of liquid bridge between the plate and the spine in the field of view during the first ∼ 8 min, as it is shown in the figure S4. In the first figure we can see the bridge formed in the left half and in the second that it fully wets the spine. Given the higher thermal conductivity of water compared to air, we expect the spine temperature to be reasonably close to the plate one.